

Magnetohydrodynamic Disc Winds and Line Width Distributions.II

L. S. Chajet¹ ^{*} and P. B. Hall¹

¹*Department of Physics and Astronomy, York University, Toronto, Ontario M3J 1P3, Canada*

Accepted XXX. Received YYY; in original form ZZZ

ABSTRACT

We study AGN emission line profiles combining an improved version of the accretion disc-wind model of Murray & Chiang with the magneto-hydrodynamic model of Emmering et al. (1992). Here we extend our previous work to consider central objects with different masses and/or luminosities. We have compared the dispersions in our model C IV linewidth distributions to observational upper limit on that dispersion, considering both smooth and clumpy torus models. Following Fine et al., we transform that scatter in the profile line-widths into a constraint on the torus geometry and show how the half-opening angle of the obscuring structure depends on the mass of the central object and the accretion rate.

We find that the results depend only mildly on the dimensionless angular momentum, one of the two integrals of motion that characterise the dynamics of the self-similar ideal MHD outflows.

Key words: galaxies: active – galaxies: nuclei – (galaxies:) quasars: emission lines

1 INTRODUCTION

Broad emission lines (BELs) are a spectral signature of Type 1 Active Galactic Nuclei (AGNs). Lines due to high-ionized species are generally single-peaked and blueshifted with respect to the systemic velocity (e.g., Sulentic et al. 1995, 2000; Vanden Berk et al. 2001). Although photoionization is well determined as the primary physical mechanism for their production, a detailed description of the region where the BELs originate is still an open question (e.g., Chelouche & Zucker 2013; Grier et al. 2013; Sluse et al. 2011). As the BLR is spatially unresolved, its structure and dynamics remain unclear and it is only through indirect methods that it can be studied.

Reverberation mapping (RM) is one of the few available such methods. It relies on the time lag in the response of the BLR to variability of the continuum (see, e.g., the review by Peterson 2006). In particular, RM studies in several AGNs have shown that the BLR is a stratified structure (e.g., Peterson & Wandel 2000): within the same AGN, the high-ionization lines are produced closer to the central source than the low-ionization lines.

Among the different competing and/or complementary models that have been developed to explain the nature of the BLR are discrete clouds and disc winds (see brief reviews by e.g., Eracleous 2006; Everett 2007). Broad-line cloud models

describe this region as composed of numerous optically-thick clouds that, photoionized by the continuum-source emission, are the emitting entities responsible for the observed lines. This model successfully explains many of the observed spectral features, but also leaves several unsolved issues, such as the formation and confinement of the clouds.

In models of outflowing gas, two major accelerating mechanisms have been invoked: magnetohydrodynamic (MHD) driving (e.g., Blandford & Payne 1982; Emmering et al. 1992; Contopoulos & Lovelace 1994; Kazanas et al. 2012), and radiative acceleration (e.g., Murray et al. 1995; Kurosawa & Proga 2009). In some of these wind models the flow is assumed to be continuous (e.g., Königl & Kartje 1994; Murray & Chiang 1997), while in others it contains embedded inhomogeneities or clouds (e.g., Bottorff et al. 1997). Both of these types of models have had some success in fitting AGN observations. The spectral line shapes can be used as a tool to study the kinematics and physics of plasmas in AGNs. One additional important motivation of wind BLR models is that they provide a feasible feedback mechanism to the host galaxy, thus regulating the co-evolution suggested by the solid relationships observationally found between the mass of the central object and some of the galaxy properties (e.g., Marconi & Hunt 2003; Häring & Rix 2004; Gültekin et al. 2009). It is also worth mentioning that the wind scenario offers the explanation least conflicting with the existence of a small group of AGN that show double-peaked line profiles (generally,

* E-mail: lchajet@yorku.ca

Balmer lines) in their spectra and with the fact that some among them fluctuate between a double- and a single-peaked profile (e.g., Flohic et al. 2012; Eracleous & Halpern 2003). In addition, the model high-velocity component of the wind naturally explains the existence of blueshifted broad absorption lines seen in an optically selected subset of the quasar population, known as broad absorption line (BAL) quasars (Murray et al. 1995; Elvis 2000).

Because broad emission lines are produced close to the central engine, they carry important information on that region of the phenomenon (Sulentic et al. 2000). Hence, accurate emission line models are important for studying AGN properties, such as black hole masses and accretion rates and put constraints on the unification paradigm. Indeed, due to their ubiquity, some authors (e.g., Richards 2012) regard emission lines as a more powerful tool to studying AGN than absorption lines, because the latter are only present in a fraction of the quasar population.

We study AGN emission line profiles combining an improved version of the accretion disc wind model of Murray & Chiang (1997) with the magnetohydrodynamic (MHD) driving of Emmering et al. 1992. Here we present the extension of our previous work in Chajet & Hall (2013, Paper I hereafter), considering a range of masses and luminosities. We have compared the averages in our model C IV linewidth distributions to the observational results of Fine et al. (2010), considering a smooth torus model. Additionally, we performed a similar study considering a clumpy torus (Nenkova et al. 2008).

The plan of the paper is as follows. In Section 2 we review our modifications to the Murray & Chiang (1997) disc-wind model. In Subsection 2.1 we outline the basics of MHD winds, with emphasis on the description of Emmering et al. (1992) and show how we constructed our combined model. Section 3 presents the C IV line profiles obtained with this model, and discusses their characteristics. In Section 4, using observational constraints on the dispersion of the line-widths, we derive constraints on the putative torus applicable to the various combinations of mass and Eddington ratio that we have considered. We explore both homogeneous (4.2) and clumpy torus (4.3) prescriptions as the obscuring structure. In section 5 we discuss how different values of the dimensionless angular momentum parameter λ affect the results. We have considered two different values of λ and run simulations using $\lambda = 10$ and $\lambda = 30$. These values were chosen to match those used by Blandford & Payne (1982) and Emmering et al. (1992), respectively. In Section 6 we discuss our results and outline some possible ways for future exploration or improvement and in Section 7 we present our conclusions.

2 MODEL DESCRIPTION

In Paper I we presented our hybrid model, that combines the disc-wind model of Murray & Chiang (1997, hereafter MC97) with the MHD driving of Emmering et al. (1992) and here we include a brief description of it, that is applied to generate emission lines from AGNs.

We assume an azimuthally symmetric, time-independent disc and wind. The lines arise at the base z_{em} of an emission region of thickness $l_{\text{em}} \ll z_{\text{em}}$, at an angle β

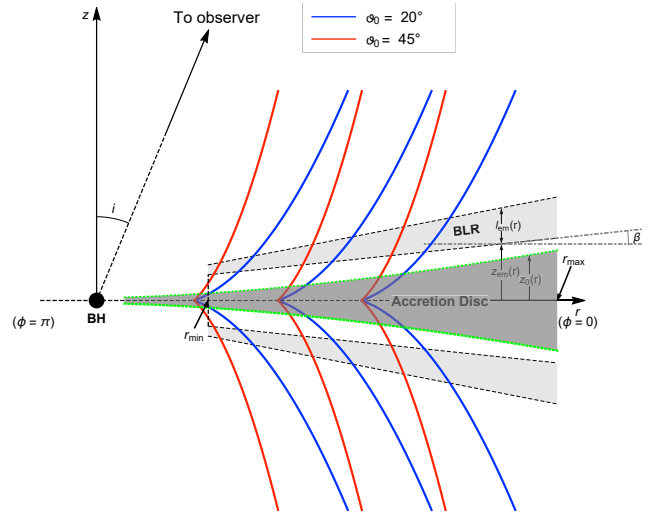


Figure 1. Streamlines for two different launch angles: $\vartheta_0 = 20^\circ, 45^\circ$. The disc midplane is assumed to lie in the $z = 0$ plane and the disc is assumed to be opaque, such that the observer, at an angle i from the $+z$ axis, sees only the upper quadrants. The lower dashed line represents the base of the emitting region, tilted by an angle β with respect to the disc plane. The BLR is a layer of thickness $l_{\text{em}}(r)$ beginning a distance $z_{\text{em}}(r)$ above the disc midplane and spanning radii $r_{\text{min}} < r < r_{\text{max}}$. The height of the disc continuum photosphere is $z_0(r)$, where r is the cylindrical radial coordinate. The disc wind lies at $z(r) > z_{\text{em}}(r)$, and the emitting region for a given line is near the base of the wind, at $z_{\text{em}}(r) < z < z_{\text{em}}(r) + l_{\text{em}}(r)$ above the disc midplane.

of the disc plane. This angle can, in principle, be a function of the radius, but we have adopted a fixed value. The wind streamlines make an angle of $\vartheta(r, z)$ relative to the disc plane.

Figure 1 depicts the system geometry and shows streamlines for two different launch angles.

The line luminosity is given by

$$L_\nu(i) = \int_{r_{\text{min}}}^{r_{\text{max}}} S_\nu(r) \frac{r}{\cos \beta(r)} dr \int_0^{2\pi} \cos \iota(r, \phi, i) \times (1 - \exp[-\tau(r, \phi, i) \times e_\nu(r, \phi, i) \times e^{-x_\nu^2(r, \phi, i)}]) d\phi \quad (1)$$

where

$$\tau(r, \phi, i) \equiv \frac{ck_0(r)/2\nu_0}{\sqrt{Q^2(r, \phi, i) + q_{\text{tt}}^2(r, \phi, i)}}, \quad (2)$$

$$e_\nu(r, \phi, i) \equiv \text{erfc} \left(-\frac{\nu - \nu_{\text{D}}(r, \phi, i)}{\sqrt{2}\Delta\nu_{\text{tt}}\sqrt{1 + q_{\text{tt}}^2(r, \phi, i)/Q^2(r, \phi, i)}} \right), \quad (3)$$

$$x_\nu^2(r, \phi, i) \equiv \frac{1}{2} \left(\frac{\nu - \nu_{\text{D}}(r, \phi, i)}{\Delta\nu_{\text{tt}}\sqrt{1 + Q^2(r, \phi, i)/q_{\text{tt}}^2(r, \phi, i)}} \right)^2 \quad (4)$$

and erfc is the complementary error function. The local inclination angle $\iota(i, r)$, that accounts for the different effective inclination that different portions of the emitting region have with respect to the line of sight (LoS), is defined by

$\cos \iota = \cos i \cos \beta - \cos \phi \sin i \sin \beta$. The factor $k_0(r) \propto n(r)$ in expression (2) is the integrated line opacity (in units of Hz/cm), where $n(r)$ is the hydrogen number density evaluated at z_{em} . For the radial dependence of the density, we adopted $n(r) = n(r_{\text{min}}/r)^2$ (Murray & Chiang 1998, MC98 hereafter). The term Q in Equations (2) to (4) is a quadratic form that determines the projection of the gradient of the wind velocity along the LoS (e.g., Rybicki & Hummer 1978, 1983), according to

$$Q \equiv \hat{\mathbf{n}} \cdot \mathbf{A} \cdot \hat{\mathbf{n}}, \quad (5)$$

where $\hat{\mathbf{n}}$ is the unit vector in the LoS direction and \mathbf{A} is the strain tensor. The Doppler-shifted central frequency of the line emitted towards the observer from location (r, ϕ) on the emitting surface is defined by $\nu_{\text{D}} = \nu_0(1 + \mathbf{v}_{\text{D}}/c)$, where c is the speed of light in a vacuum.

Expressions (2) to (4) include also the term ‘thermal Q ’, a quantity defined as the ratio of the characteristic thermal (\mathbf{v}_{th}) plus turbulent velocity (\mathbf{v}_{turb}) of the ion to the thickness of the emitting layer along the LoS: $q_{\text{tt}}(r, \phi, i) = \mathbf{v}_{\text{tt}} \cos \iota(r, \phi, i)/l_{\text{em}}(r) \cos \beta$, with $\mathbf{v}_{\text{tt}}^2 \equiv \mathbf{v}_{\text{th}}^2 + \mathbf{v}_{\text{turb}}^2$. The turbulence is assumed to be isotropic. The effective frequency dispersion of the line is evaluated according to $\Delta \nu_{\text{tt}} = \nu_0 \mathbf{v}_{\text{tt}}/c$ and the emission region thickness is given by

$$l_{\text{em}}(r) = 0.1 z_{\text{em}} \left[\frac{\mathbf{v}_{\text{tt}} + \mathbf{v}_{\text{p}}(r, z_{\text{em}})}{\mathbf{v}_{\text{tt}} + \mathbf{v}_{\infty}(r, z_{\text{em}})} \right], \quad (6)$$

where $\mathbf{v}_{\text{p}}(r, z)$ and $\mathbf{v}_{\infty}(r, z)$ are the instantaneous and terminal poloidal velocities, respectively, of the wind along the streamline at (r, z) . The z -dependent quantities are evaluated at z_{em} .

The dependences of the quantities $q_{\text{tt}}(r, \phi, i)$ and $Q(r, \phi, i)$ on the different parameters are rather complex to make a clear comparison in the general case. We will, then, discuss this point in Section 3.

2.1 Ideal MHD wind launching

Magnetic acceleration of outflows has been often suggested in the literature as an efficient means of removing excess of angular momentum from the accreting material (e.g., Blandford & Payne 1982; Contopoulos & Lovelace 1994; Königl & Kartje 1994; Everett 2005). The standard non-relativistic ideal magneto-hydrodynamic (MHD) wind equations are presented in (e.g.) the above mentioned references, as well as in Paper I. In steady state (i.e. $\partial/\partial t = 0$) and assuming axisymmetry (i.e. $\partial/\partial \phi = 0$), the solutions have a number of conserved quantities along each magnetic field line (e.g., Mestel 1968), that impose constraints to the flow dynamics. These are the mass to magnetic flux ratio, $\frac{k}{4\pi} = \frac{\rho \mathbf{v}_{\text{p}}}{B_{\text{p}}}$; specific angular momentum, $l = r \left(\mathbf{v}_{\phi} - \frac{B_{\phi}}{k} \right)$ and specific energy, $e = \frac{\mathbf{v}^2}{2} + h + \Phi_{\text{g}} - \frac{r\Omega B_{\phi}}{k}$, where the subscripts p and ϕ correspond respectively to the poloidal and azimuthal components of the velocity, \mathbf{v} , and magnetic, \mathbf{B} , vector fields; ρ is the gas density; Φ_{g} , the gravitational potential; and h and Ω are the specific enthalpy and the angular velocity, respectively.

An important quantity defined for magnetized fluids is the so-called Alfvén Mach number. The square of this quantity is defined as $m = \mathbf{v}_{\text{p}}^2/\mathbf{v}_{\text{Ap}}^2$, where \mathbf{v}_{Ap} is the poloidal component of the Alfvén velocity $\mathbf{v}_{\text{A}} = \frac{B}{\sqrt{4\pi\rho}}$ which is the

characteristic velocity of the propagation of magnetic signals in an MHD fluid. The Alfvén radius r_{A} is the point on each poloidal field line where $m = 1$; the loci of all r_{A} define the Alfvén surface. The subscript ‘‘A’’ refers, hereafter, to quantities evaluated at the Alfvén point.

2.1.1 Blandford & Payne MHD Wind Solution

Analytic solutions for the system of equations that defines the stationary ideal MHD problem can be obtained only under some simplifying assumption such as self-similarity (e.g., Blandford & Payne 1982, BP82 hereafter). This solution for the field can be written in terms of variables χ , $\xi(\chi)$, ϕ , and r_0 , which are related to the cylindrical coordinates via

$$\mathbf{r} \equiv [r, \phi, z] = [r_0 \xi(\chi), \phi, r_0 \chi], \quad (7)$$

where the adopted independent variables (r_0, χ) are a pair of spatial coordinates analogous to (r, z) . The function $\xi(\chi)$ describes the shape of the field lines and, in the general case, is not *a priori* known, but found as part of a self-consistent solution to the MHD equations. The flow velocity components are given by

$$\mathbf{v} = [\xi'(\chi)f(\chi), g(\chi), f(\chi)] \sqrt{\frac{GM}{r_0}}, \quad (8)$$

where a prime denotes differentiation with respect to χ , and G and M are respectively the gravitational constant and the mass of the central black hole.

The self-similar scaling of the magnetic field amplitude B , and gas density ρ with the spherical radial coordinate r is given, in the general case (e.g., Emmering et al. 1992; Contopoulos & Lovelace 1994; Kazanas et al. 2012), by $\rho \propto r_0^{-b}$, for which $B \propto r_0^{-(b+1)/2}$. The BP82 solution is a particular case corresponding to $b = 3/2$. The magnetic field and density at arbitrary positions can be then written, in accordance with the self-similarity *Ansatz* (Equation (7)), as $\mathbf{B} = B_0(r_0)\mathbf{b}(\chi)$ and $\rho = \rho_0(r_0)\varrho(\chi)$. On the disc plane the rotational velocity, \mathbf{v}_{ϕ} , is Keplerian and scales as $\mathbf{v}_{\phi} \propto r_0^{-1/2}$. The functions $\xi(\chi)$, $f(\chi)$ and $g(\chi)$ have to satisfy the flow MHD equations subject to the above scalings of ρ , B , and \mathbf{v}_{ϕ} and boundary conditions. In particular, at the disc surface $\xi(0) = 1$, $f(0) = 0$ and $g(0) = 1$.

The parameters of the model are the dimensionless expressions of the integrals of motion: $\epsilon = e/(GM/r_0)$, $\lambda = l/(GMr_0)^{1/2}$ and $\kappa = k(1 + \xi_0'^2) \left[(GM/r_0)^{1/2}/B_0 \right]$. An extra parameter is the value of the derivative ξ_0' of the self-similar function ξ at the disc surface. However, due to the regularity conditions that must be satisfied, these parameters are not independent. In particular, the value of $\xi_0' \equiv \xi'(\chi = 0)$ must be chosen to ensure the regularity of the solution at the Alfvén point. That reduces the degrees of freedom of the solutions, that are then parametrized by two numbers.

BP82 studied outflows that become super-Alfvénic (i.e., $m > 1$) at a finite height above the disc. The asymptotic conditions for such flows admit two kind of solutions that depend on the location of the fast-mode Mach number n above the disc.

The family of solutions that asymptotically approach $n = 1$ as $\chi \rightarrow \infty$ have the generic form $\xi = c_1 \chi^\alpha$, where

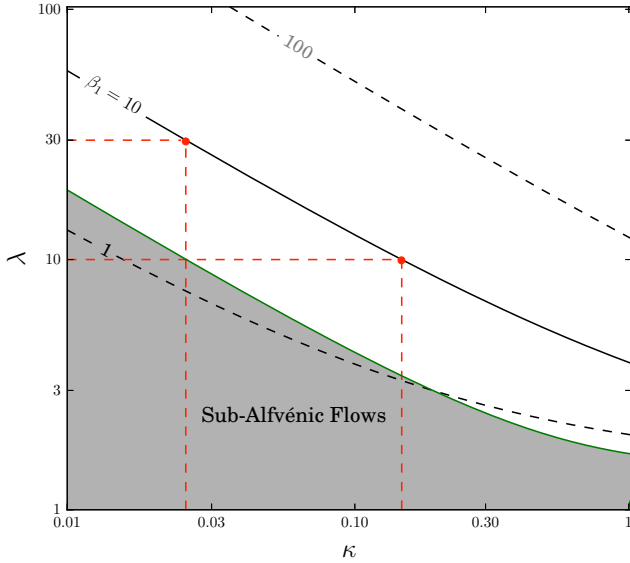


Figure 2. Contour plot analogous to Fig. 2 of [Blandford & Payne \(1982\)](#). Each contour corresponds to a value of the quantity β_1 , defined in Equation (9), that is fixed for a given problem. The solid contour corresponds to $\beta_1 = 10$ and the possible (κ, λ) pairs for our problem, set by the condition in Equation (12) imposed by the [Emmering et al. \(1992\)](#) choice of parameters. The dashed red lines locate the two points (also marked in red) for which we have explored in this work. Flows in the grey-shadowed region satisfy the condition $\kappa\lambda_{\min}(2\lambda_{\min} - 3)^{1/2} < 1$, and will never become super-Alfvénic ($4\pi\rho v_p^2 > B_p^2$).

c_1 and $\alpha = 1 - 3^{3/2}/\beta_1$ are constants, controlled by the parameter

$$\beta_1 \equiv \kappa(2\lambda - 3)^{3/2} \gg 1. \quad (9)$$

Figure 2 (similar to Figure 2 in BP82) depicts the contours of constant β_1 for three different values of the parameter.

The asymptotic value of the function f is given by

$$f_\infty = \left(\frac{2\lambda - 3}{3}\right)^{1/2}. \quad (10)$$

2.1.2 *Emmering et al. model*

[Emmering et al. \(1992, EBS92 hereafter\)](#) impose *a priori* the functional form of the solution so that it will asymptotically tend to the type of [BP82](#) solution presented above. In their equation (3.19), [EBS92](#) give an explicit form for the function $\xi(\chi)$:

$$\xi = \left(\frac{\chi}{c_2} + 1\right)^{1/2}, \quad (11)$$

where $c_2 = \frac{1}{2} \tan \vartheta_0$ was chosen to ensure that the field lines make an initial angle ϑ_0 with the disc plane, so that $\cot \vartheta_0 = \xi'_0$ and the subscript 0 means that the quantities are evaluated at the disc plane. It can be shown (e.g., [BP82, Heyvaerts 1996](#)) that this angle must satisfy the condition $\vartheta_0 < 60^\circ$.

For the form proposed by [EBS92](#), the only possible value of β_1 is $6\sqrt{3} \sim 10$. Replacing this value in Equation (9) gives that, as shown by [EBS92](#), for this kind of solution the

parameters κ and λ must be related by:

$$\kappa = 2 \left(\frac{3}{2\lambda - 3}\right)^{3/2} \quad (12)$$

Thus, in this model the solutions depend on λ and ϑ_0 .

The [EBS92](#) work was intended to support the cloud scenario of the BLR, and thus the authors proposed that the emission lines arise in clouds confined by an MHD flow. However, we follow [MC97](#) and [MC98](#) in assuming that the lines form in a continuous medium. We consider line emissivity obtained by a [CLOUDY](#) photoionization model, different from either of the emissivity laws adopted by [EBS92](#). Two of those emissivity models include electron scattering, which is not considered in our model. In [EBS92](#) both the dimensionless angular momentum λ and the launch angle are fixed. We, on the other hand, varied those parameters to study their effect on the profiles. Note also that, while [EBS92](#) obtains the line luminosity integrating in the two poloidal variables, we include the z -integral in the optical depth expression, already incorporated in Equation (2).

3 LINE PROFILES

In [Paper I](#) we applied the modified model described above to our fiducial case, characterised by mass $M = 10^8 M_\odot$ and luminosity L_{1350} (defined below) $10^{46} \text{ erg s}^{-1}$, and considered a dimensionless specific angular momentum $\lambda = 10$. We then studied several combinations of inclination angles, in the range $5^\circ \leq i \leq 84^\circ$ and launch angles $6^\circ \leq \vartheta_0 < 60^\circ$. The maximum viewing angle was set as to be the angle at which an observer would see the base of the emitting region, that was chosen to make an angle $\beta = 6^\circ$ from the disc plane. In the present work we analyse, for the same set of viewing and launch angles, how the emission line profiles for different masses and luminosities are effected. For each of such combinations, the specific luminosity from each component of the C IV doublet is computed separately, and then the results added together.

To scale the inner and outer radii of the emitting region from the fiducial case to any mass-luminosity combination we adopted a luminosity- and mass-based scaling:

$$r_{\min, \max} = 2M_8^{1/3} L_{46}^{0.5} 10^{15, 19} \text{ cm}, \quad (13)$$

where $M_8 = \frac{M}{10^8 M_\odot}$ and $L_{46} = \frac{L_{1350}}{10^{46} \text{ erg s}^{-1}}$ and M is the mass, in units of solar masses and L_{1350} is the object's UV luminosity, in erg s^{-1} . We had initially set a scaling depending only on luminosity, $r_{\min, \max} = 2L_{46}^{0.5} 10^{15, 19} \text{ cm}$. However, the profiles rendered by such a scaling were too broad and had much larger linewidth dispersions than the fiducial case. Incorporating the mass dependence to the scaling had the effect of reducing both the FWHMs and corresponding dispersions. A mass-dependent scaling has been applied before (in the optical by e.g., [Flohic et al. 2012](#)). In that work, the computational domain (inner and outer radii of the BLR) is given in units of the gravitational radius of the central object, $R_G = GM/c^2$. The mass scaling adopted here is motivated by the results on the BLR reported by [Elitzur et al. \(2014\)](#).

As discussed in [Paper I](#), we determined the source function for our simulations by applying the RM results

of Kaspi et al. (2007) to the radial line luminosity function $L(r)$ calculated by MC98 for a quasar with $L_{1350} \equiv \nu L_\nu(1350 \text{ \AA}) = 10^{46} \text{ erg s}^{-1}$ and shown in their Figure 5b. The radii in the MC98 Figure 5b line luminosity function have been empirically adjusted down by a factor of five to match the RM results of Kaspi et al. (2007). Other relevant physical parameters are the density and density power-law exponent and thermal plus turbulent velocity, chosen to be $n_0 = 10^{11} \text{ cm}^{-3}$, $b = 2$ and $v_{\text{tt}} = 10^7 \text{ cm s}^{-1}$, respectively, same as the corresponding values used in Paper I.

We are now in position to compare the quantities $q_{\text{tt}}(r, \phi, i)$ and $Q(r, \phi, i)$. As mentioned above, a general description is not possible, but we can discuss the limiting cases that we have identified. Running our code for a number of combinations of relevant parameters shows that the behaviour of the ratio $R_{\text{Qq}} = \left| \frac{Q(r, \phi, i)}{q_{\text{tt}}(r, \phi, i)} \right|$ depends strongly on ϑ_0 . For small values of ϑ_0 ($\lesssim 30^\circ$), and given i , the ratio is a strong function of the radius, with some azimuthal modulation at any given radius. The azimuthal modulation level decreases with decreasing inclination. For the smallest inclinations ($i \lesssim 10^\circ$), there is a turnover radius beyond which the overall dominant factor changes. For example, the $(\vartheta_0, i) = (6^\circ, 10^\circ)$ combination gives $1 \lesssim R_{\text{Qq}} \lesssim 53$ for most ($\sim 2/3$) of the radial domain and $0.17 \lesssim R_{\text{Qq}} \lesssim 1$ for the largest radii.

On the contrary, for large values of ϑ_0 ($\gtrsim 30^\circ$), the dominant factor in R_{Qq} is q_{tt} . As an example, for $(\vartheta_0, i) = (45^\circ, 10^\circ)$ R_{Qq} lies in the range $0.0031 \lesssim R_{\text{Qq}} \lesssim 0.17$. Exact values of the ratio depend on the radius and increase with increasing i . The azimuthal modulation is only important at large inclination values ($i \geq 45^\circ$). Although the values reported correspond to the fiducial case, the qualitative description is correct for the different masses and accretion rates studied.

The line profiles are determined by the kinematics and geometry of the gas distribution in the emission region. The inner and outer radii of that region, defined by Equation (13), can be recast to show the dependence on the accretion rate. Figures 3 to 5 show several profiles obtained in our simulations. The difference from one figure to the other is the value of the accretion rate, as shown by the inside legend. The Eddington ratio, that measures the accretion rates in Eddington units, is defined as $\dot{m} = L_{\text{Bol}}/L_{\text{Edd}}$, where L_{Edd} is the Eddington luminosity given by $L_{\text{Edd}} = 1.26 \times 10^{46} \text{ erg s}^{-1}$ ($M_{\text{BH}}/10^8 M_\odot$).

Each panel of these figures includes the lines corresponding to fixed viewing and launch angles and luminosities, as described in the caption to Figure 3. Solid and dashed lines correspond to $\lambda = 10$ and 30 , respectively. The normalization is with respect to the corresponding $\lambda = 10$ case and only results corresponding to a subset of the viewing angles in the simulations are included. We postpone until section 5 the discussion on how different λ values affect the results. The velocities in the x -axes represent velocities from the observer's point of view, therefore negative velocities correspond to blueshifts. The zero velocity, marked by a vertical dashed line in each panel, is the average of the two doublet wavelengths.

Within each panel, not only the profiles are broader with increasing mass and decreasing luminosity, but also the shift of the peak and the fractions of the flux blue- and red-

ward of the central velocity vary. For fixed ϑ_0 , the profiles are broader as the inclination angle increases. The dependence of the line-profile width on mass and luminosity can be seen by considering the Keplerian speed $v_{\text{K}} \sim \sqrt{M/r}$ and using Equation (13) to express $r \sim M^{1/3} L^{1/2}$, we find that $v_{\text{K}} \sim M^{1/3} L^{-1/4}$. The profiles corresponding to any mass-luminosity combination have similar general behaviour and trends to the fiducial case, analysed in Paper I. For instance, all profiles have a certain degree of asymmetry that decreases with increasing inclination. As before, the blue wings change less than the red wings, so that as the inclination angle increases, the red wings become relatively stronger.

Physically the wind velocity depends on the launch angle, but the observer sees the fraction projected onto the LoS. However, as discussed in Paper I, in the framework of the present model, the actual angle to be considered is the angle ϑ at which a line launched with some ϑ_0 crosses the base of the emitting region (when ϑ_0 increases, so does ϑ). For any given combination of the two angles i and ϑ_0 , the projection of the velocity will be towards the observer on the fractions of the emitting region that satisfy the condition $\vartheta > i$. The velocity relevant for producing the observed line profiles is the Doppler velocity, that includes a contribution from the rotational velocity. As ϑ increases, the rotational velocity becomes increasingly dominant, producing more symmetric profiles. For any launch angle, the relative importance of the receding term with respect to the approaching term increases with increasing viewing angle, but the effect is larger for smaller ϑ_0 .

The shape of a spectral line can be characterised by analysing the ratio $S = \text{FWHM}/\sigma_1$, where σ_1 is the standard deviation of the line. For a Gaussian profile, $S_{\text{Gauss}} = 2\sqrt{2 \ln(2)} \simeq 2.35$, while $S \rightarrow 0$ for Lorentzian and logarithmic profiles. For our results we find minimum and mean S values ~ 0.69 and ~ 1.33 respectively.

Figure 6 shows the distribution of the parameter S for our profiles as a function of two different line-width measures: FWHM in the right and σ_1 in the left. The fact that most of our lines are below the S_{Gauss} value, indicates that they have more prominent wings than a simple Gaussian profile. This is not surprising, as the dynamics is dominated by the turbulent plus thermal velocity.

4 FWHM STATISTICS

Here we explore the FWHM of our profiles in relation to the luminosity of the sources and then consider the dispersion of this line-width characterisation. Using the FWHM allows a fairly simple comparison to the observational data and constraints reported by Fine et al. (2010), who used inter-percentile values (IPV) to characterise the line-widths, and an immediate possibility of extension to other works in the literature.

Figure 7 shows the $\log(\text{FWHM})$ of the line profiles from our simulations. Each panel corresponds to a given mass and luminosity and each colour, to a different launch angle, with solid and dashed lines used for the $\lambda = 10$ and $\lambda = 30$ cases respectively. Here we can see again that the results follow the expected behaviour of the FWHM with mass and luminosity, i.e., the FWHM increases with increasing mass and decreasing luminosity.

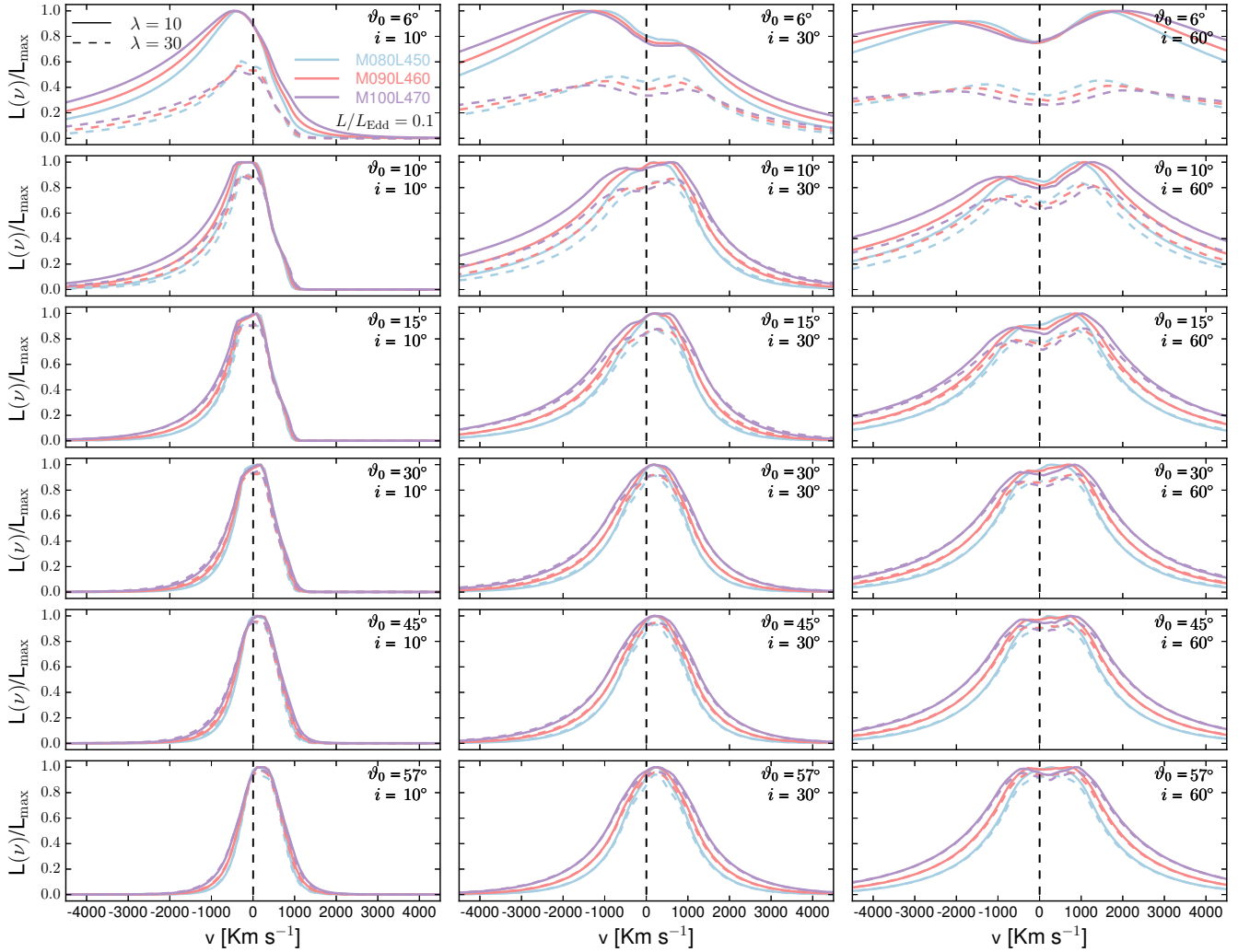


Figure 3. Normalized (with respect to the corresponding $\lambda = 10$ case profile) line luminosity vs. velocity for several values of viewing and launch angles. Each panel shows the profiles for given launch and viewing angles. Along rows, launch angles are constant, and viewing angles increase from left to right. Only profiles corresponding to three viewing angles ($i = 10^\circ, 30^\circ, 60^\circ$) are shown. The labels indicate $\log M_i$ and $\log L_i$, where M_i is the mass of the central BH in the corresponding simulation, in units of solar masses, and L_i is the assumed luminosity in erg s^{-1} . For example, M080L450 indicates $\log M_i = 8.0$ and $\log L_i = 45.0$. This set of lines correspond to the case $L/L_{\text{Edd}} = 0.1$.

Notably, for any given mass and luminosity (i.e., within a particular panel), the differences due to the angular momentum are almost independent of the launch angle, except for the lowest ϑ_0 value. As mentioned, detailed discussion on this matter is placed in section 5.

4.1 Luminosity-linewidth plane

Figure 8 is similar to Figure 2 from Fine et al. (2010). The grey-shaded area corresponds approximately to the densest region in that figure. We recall here again that we used line FWHM (instead of IPV) and in the x -axis, luminosities have been plotted, instead of absolute magnitudes. The dotted and dashed lines represent loci of constant mass and Eddington ratio, respectively, where the mass has been evaluated, as Fine et al. (2010), using Equation (7) in Vestergaard & Peterson (2006, VP06, hereafter), repro-

duced below:

$$\log M_{\text{BH}}(\text{C IV}) = \log \left\{ \left[\frac{\text{FWHM}(\text{C IV})}{1000 \text{ km s}^{-1}} \right]^2 \left[\frac{\lambda L_\lambda(1350 \text{ \AA})}{10^{44} \text{ erg s}^{-1}} \right]^{0.53} \right\} + (6.66 \pm 0.01). \quad (14)$$

The shaded regions are bound by lines of constant $\log(M_i) \pm 0.2$, where M_i is one of the mass values used in our simulations, in units of solar masses. While the sample standard deviation of the weighted average zero point of their mass scaling relationships reported by VP06 is 0.36 dex, we used a smaller range around $\log M_i$ to avoid overlapping of regions belonging to two different such values. For each mass-luminosity combination, results corresponding to the same launch angle but different inclination are linked by solid lines, with the same colour scheme used in other figures.

The differences in luminosity from sources of intrinsic

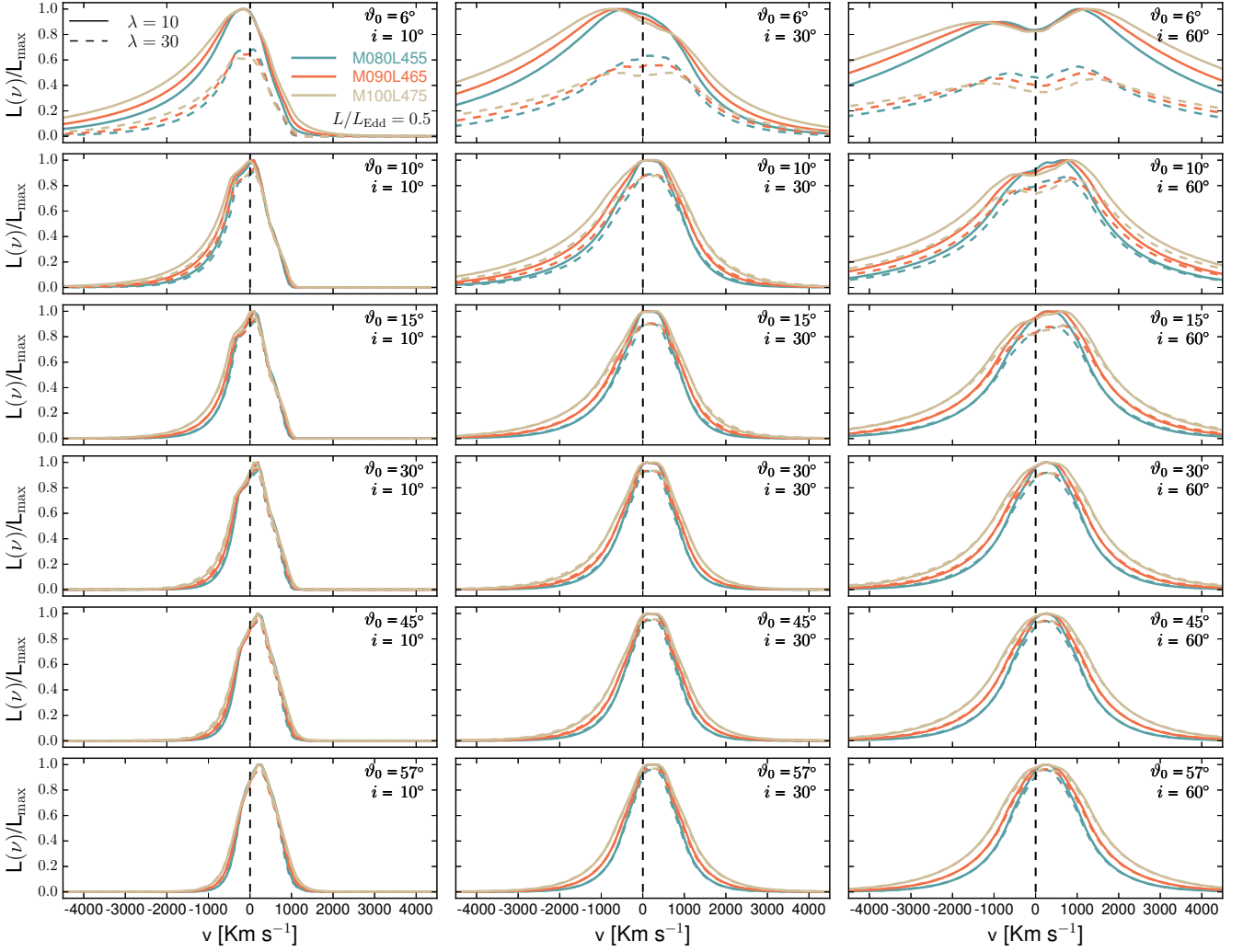


Figure 4. Normalized (with respect to the corresponding $\lambda = 10$ case profile) line luminosity vs. velocity for several values of viewing and launch angles. Similar to Fig. 3, but for $L/L_{\text{Edd}} = 0.5$.

identical luminosities are attributable to the differences in viewing angle, because the observer sees a fraction that depends on the projection on the sky of the emitting region, so the x -axis is constructed by multiplying the assumed object's luminosity by the cosine of the inclination angle.

Note that if the black hole mass were estimated using Equation (14), many of the results could not retrieve their original mass values. In general, the cases that seem best represented by the expression are in the range $8.0 \lesssim \log M_i \lesssim 8.5$, in particular for the largest viewing angles. For $\log M_i \sim 9$, fewer combinations, corresponding to the larger Eddington ratios, smaller ϑ_0 and larger i , reproduce the original mass values, whereas $\log M_i \sim 10$, no combination can retrieve their true M_{BH} . This is partly due to the fact that the expression given by VP06 does not include any angular dependency, although the issue is, in effect, analysed in their work. While the case of dependence on launch angle has not been studied, the influence of the viewing angle has been considered in several works (e.g., VP06; Collin et al. 2006; Decarli et al. 2010; Assef et al. 2011; Denney 2012). One way to compare the masses obtained by applying ,VP06

Equation 7 versus the objects' true masses is to study, for given ϑ_0 , the mean of the ratio of the two quantities up to different i_{max} values in a torus model. Figure 9 shows normalized histograms of $\langle \log(M_{\text{VP06}}/M_{\text{True}}) \rangle$, with the panels arranged according to the launch angle. The FWHM values are taken from the interpolated function. All histograms are skewed and their widths depend strongly on the launch angle. Note that the skewness direction also depends on this angle, and is positive for the smallest ϑ_0 and becomes increasingly negative as the launch angle increases. In Figure 10 we present the normalized histogram of the distribution of $\langle \log(M_{\text{VP06}}/M_{\text{True}}) \rangle$ as function of i_{max} for the whole set adopting a smooth torus model (discussed in more detail in section 4.2).

Note that the correlation between FWHM and IPV has a non-negligible scatter, as can be seen from e.g., Figure A8 of Fine et al. (2010). Moreover, there is no direct conversion from one measure to the other, except for well-determined cases, such as a Gaussian curve, for which the relation is $\text{FWHM} = 1.75 \text{ IPV}$. This degeneracy makes the comparison between our linewidth vs. lu-

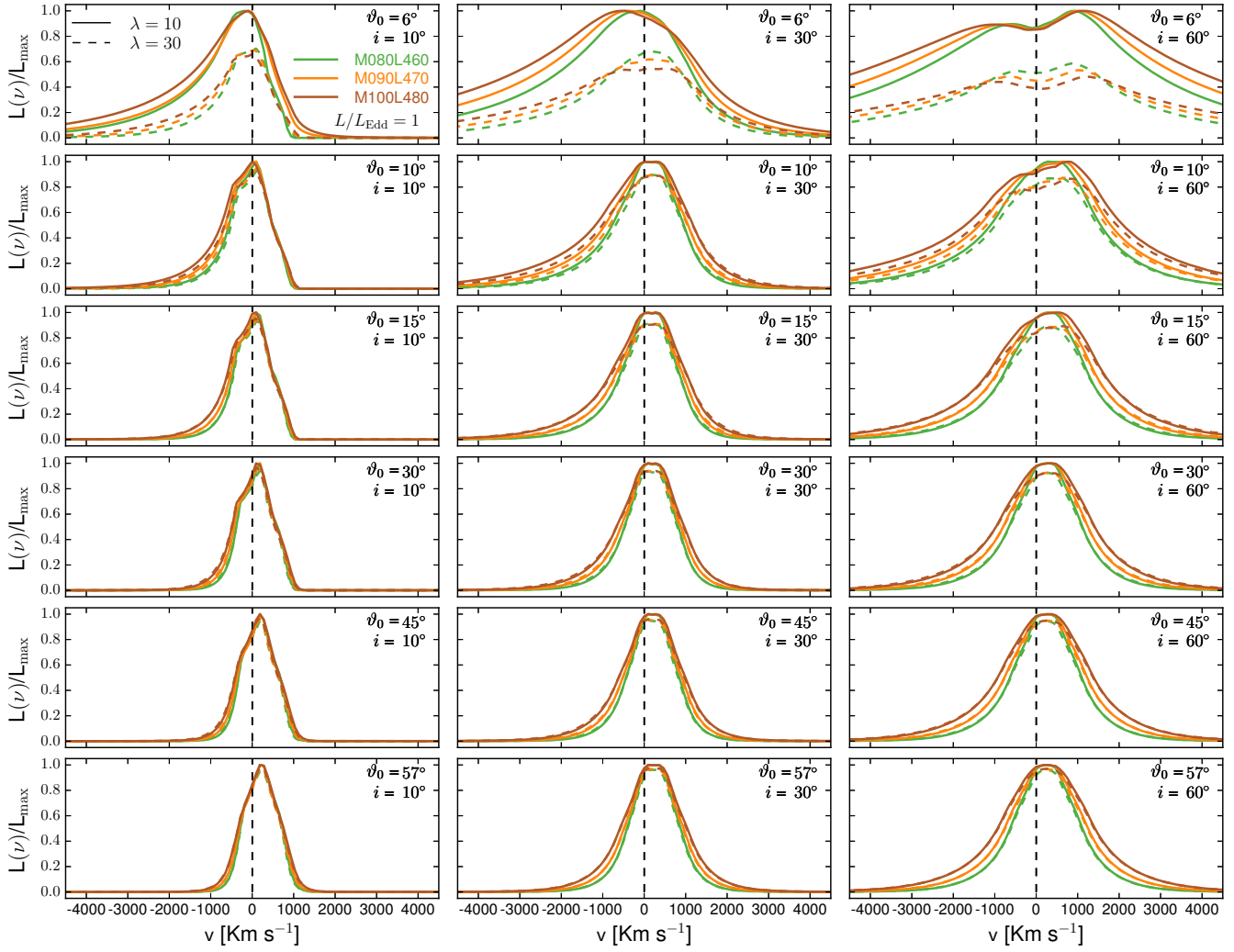


Figure 5. Normalized (with respect to the corresponding $\lambda = 10$ case profile) line luminosity vs. velocity for several values of viewing and launch angles. Similar to Fig. 3, but for $L/L_{\text{Edd}} = 1$.

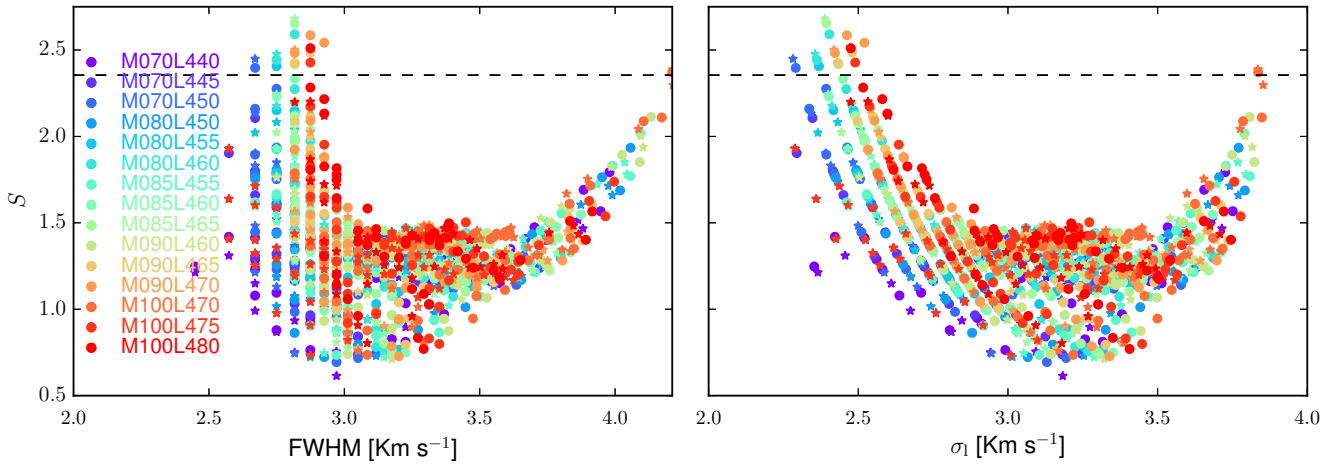


Figure 6. Line shape parameter, S vs. FWHM (left) and S vs. σ_1 for all $\lambda = 10$ profiles, with $S = \text{FWHM}/\sigma_1$, where σ_1 is the standard deviation of the line. The dashed line shown in both panels indicates $S = S_{\text{Gauss}} = 2\sqrt{2\ln(2)} \simeq 2.35$. Labels follow the scheme laid out in the caption to Figure 3.

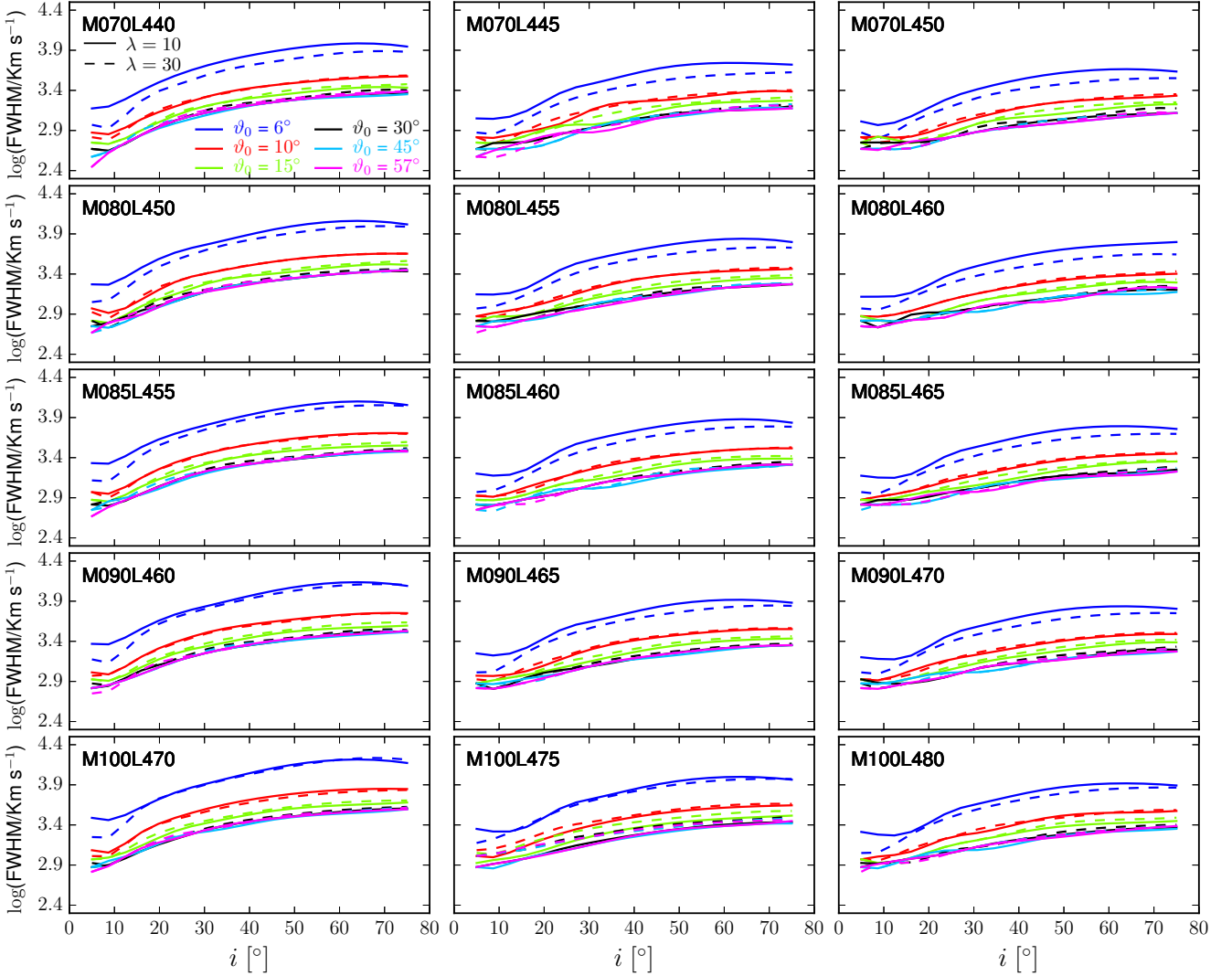


Figure 7. Profile FWHM vs. inclination angle. Solid lines are $\lambda = 10$ cases, while $\lambda = 30$ cases are represented by dashed lines. Each panel corresponds to a different combination of mass and luminosity and each line represents results for a given launch angle.

minosity with Figure 2 of Fine et al. (2010) not completely straightforward. A more direct comparison can be done with the results of Decarli et al. (2008), who reported a mean $\langle \text{FWHM} \rangle = 4030 \pm 1200 \text{ km s}^{-1}$ from their sample. This value might be consistent with our findings, although it should be pointed out that their sample was much smaller than that of Fine et al. (2010).

4.2 Dispersion of log FWHM-smooth torus

Analogous to what we did in Paper I, we also analyse the FWHM of our line profiles applying the prescription of Fine et al. (2008, 2010), who constrained the possible viewing angles using geometrical models for the BLR and comparing the expected dispersion in line-widths to their observational data. Figure 11 sketches the assumed geometry.

Using the launch angle as a parameter, we evaluate the dispersion of the function $f(i) = \log(\text{FWHM})$. For a given i_{\min} , the mean and the variance of the FWHMs are functions

of i_{\max} , according to

$$\bar{f}(i_{\max}) = \frac{\int_{i_{\min}}^{i_{\max}} \sin i P(i) f(i) di}{\int_{i_{\min}}^{i_{\max}} \sin i P(i) di}, \quad (15)$$

$$\sigma_f^2(i_{\max}) = \frac{\int_{i_{\min}}^{i_{\max}} \sin i P(i) [f(i) - \bar{f}(i_{\max})]^2 di}{\int_{i_{\min}}^{i_{\max}} \sin i P(i) di}, \quad (16)$$

where, for the case of a smooth obscuring torus, the escape probability is a step function

$$P(i) = \begin{cases} 1 & \text{for } i \leq i_{\max} \\ 0 & \text{for } i > i_{\max} \end{cases}$$

for a given i_{\max} .

Here we perform the same calculations for each of the combinations of mass and luminosity. Thus, for each set of profiles obtained for different inclination angles i and launch angles, ϑ_0 we study how the FWHMs are distributed

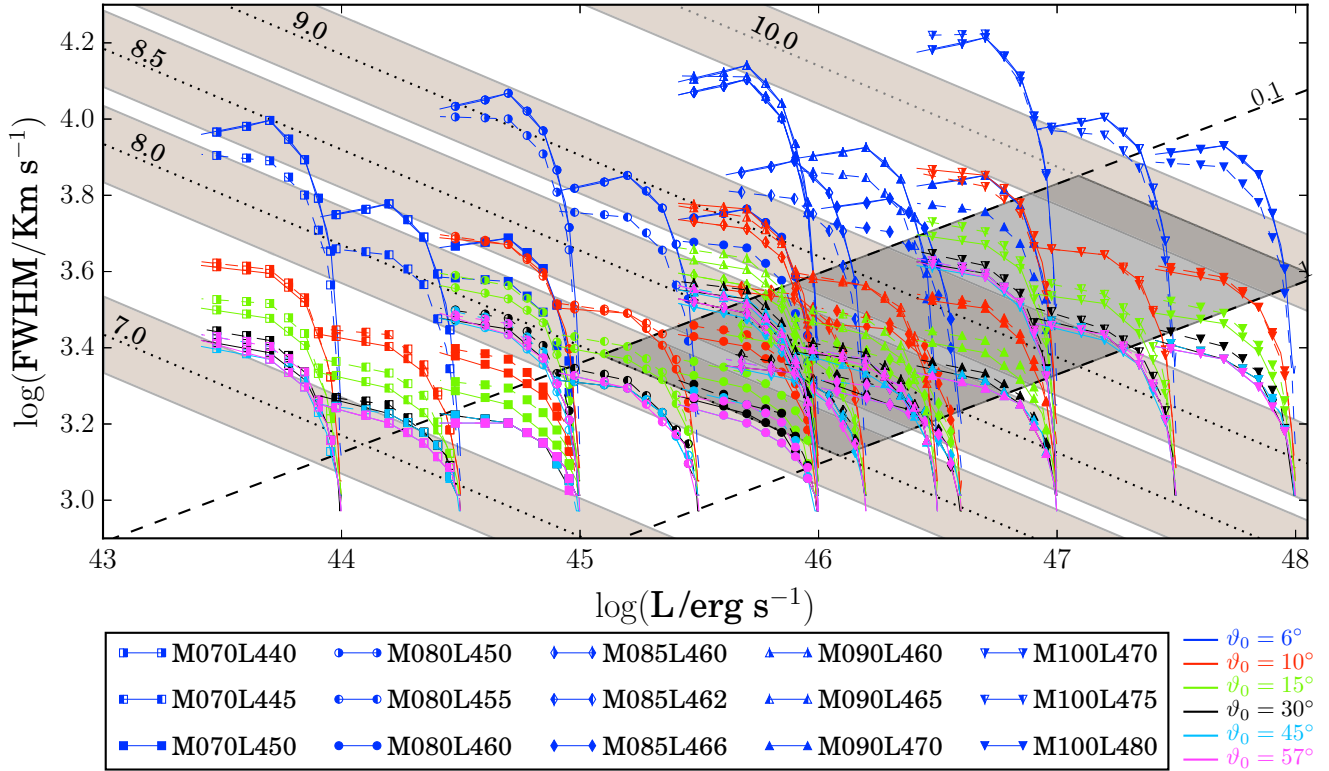


Figure 8. Similar to Figure 2 of [Fine et al. \(2010\)](#). The grey-shaded area corresponds approximately to the densest region in that figure. Note that the quantities in both axes differ from the ones used by [Fine et al. \(2010\)](#). In the x -axis, we used luminosities instead of absolute magnitudes and for the line-width measure, in the y -axis, we used FWHM instead of IPV. The dotted and dashed lines represent loci of constant mass and Eddington ratio, respectively, where the mass has been evaluated using Equation (7) in [VP06](#) (reproduced in Equation (14)). The shaded regions are bound by lines of constant $\log(M_i/M_\odot) \pm 0.2$, where M_i is one of the mass values used in our simulations. Any point in the plane represents the result from a simulation with given mass, luminosity and launch and inclination angles. Each symbol corresponds to a mass-luminosity combination, and each colour (with the same scheme used in other figures), to a launch angle. For fixed ϑ_0 the coloured solid lines join cases corresponding to different viewing angles. For any given mass-luminosity case, we see that results from the lowest ϑ_0 values are consistently larger, for fixed i , that results from any other launch angle. Furthermore, the lower the launch angle, the larger the spread in $\log(\text{FWHM})$ values.

with respect to i . For the C IV case that is of interest here, [Fine et al. \(2010\)](#) obtained an observational $\sigma_f(i_{\max}) = 0.08$ dex limit.

We show the dispersion of our line profile sets versus i_{\max} in Figure 12. The panels are arranged as constant mass along rows and constant Eddington ratio along columns, and the black horizontal dashed line in each of them represents the [Fine et al. \(2010\)](#) constraint. Only dispersions that satisfy $\sigma_f(i_{\max}) \leq 0.08$ dex are allowed, which imposes a constraint on the possible i_{\max} . In this test, the constraint on i_{\max} represents the torus half-opening angle that would yield a Type 1 object. The solid and dashed lines correspond to $\lambda = 10$ and $\lambda = 30$ cases, respectively.

The set of allowed i_{\max} changes from left to right, increasing as the Eddington ratio increases. From top to bottom, i.e., for constant Eddington ratio, the range of allowed i_{\max} values shrinks with increasing mass. These features are related to the torus geometry and its dependence on mass and luminosity and will be discussed below.

As shown in [Paper I](#) for the fiducial case, another way to visualise the constraining of the i_{\max} parameter is by making, for each mass-luminosity combination, contour plots of the corresponding $\sigma_f(i_{\max})$ as function of both ϑ_0 and i_{\max} .

In Figure 13 we show such contour plots of the standard deviation of the profile FWHM vs. launch and inclination angles for our set of masses and luminosities for the case $\lambda = 10$. The data are shown in the same arrangement as in Figure 12.

Recall that the region allowed by the [Fine et al. \(2010\)](#) result is a measure of the torus opening angle and the torus is, in the standard model, the component that determines whether an object seen under a viewing angle i is Type 1 or 2. As can be seen from Figure 13, in the present framework our upper limit on the half-opening angle of the torus of an AGN depends on both the mass and luminosity of the central engine.

If the broadening of the lines were only due to Keplerian motions modulated by the inclination dependence, the [Fine et al.](#) test would not differentiate among different mass-luminosity combinations, because that test analyses the dispersion of the logarithm of the line FWHMs rather than the FWHMs themselves. The fact that there are great differences in the allowed regions in the $i_{\max} - \vartheta_0$ plane for the different cases is a consequence of a more complex entanglement between the relevant parameters (mass, luminosity, viewing and launch angles, acceleration mechanism, etc.).

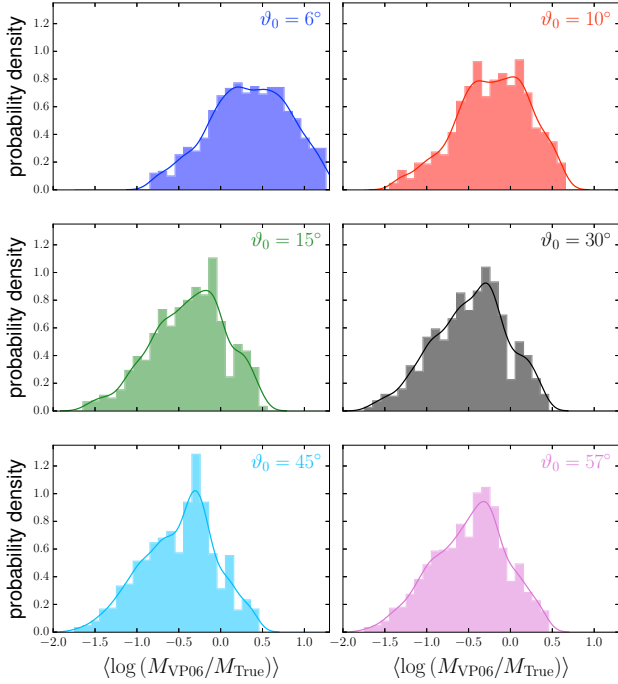


Figure 9. Normalized histograms of the quantity $\langle \log(M_{VP06}/M_{True}) \rangle$, up to a set of i_{max} values within a smooth torus model, for the different mass sets. Each panel corresponds to a given launching angle. The solid lines represent smooth histograms (kernel density estimation, KDE) over the same data. The skewness is positive in all cases, except the corresponding to $\vartheta_0 = 6^\circ$, and becomes increasingly negative as the launch angle increases.

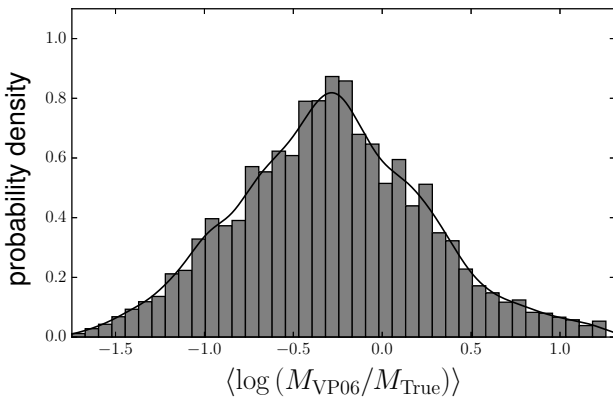


Figure 10. Normalized histograms of the quantity $\langle \log(M_{VP06}/M_{True}) \rangle$ as a function of i_{max} for all mass sets, no discriminating by launch angle or black hole mass.

Looking along each row in Figure 13 the mass is constant and the allowed regions in the $i_{max} - \vartheta_0$ plane increase in size from left to right, as the Eddington ratio increases. We would like to link this to observational results other than those of Fine et al. (2010). By construction, increasing the allowed region implies the possibility that the torus opening angle measured from the axis also increases. In the scenario under consideration (fixed mass), that would imply that more luminous objects have a higher probability of

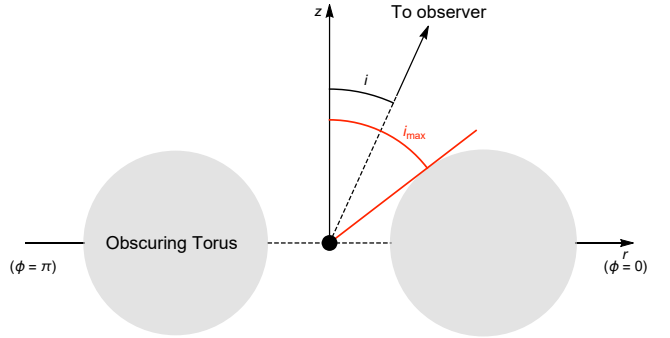


Figure 11. Torus geometry. The angle i is the observing angle to the AGN, and the opening angle i_{max} assumed to be constrained by an obscuring torus.

being observed as Type 1 than less luminous counterparts. That is, there could be more torus opening angle values under which a luminous object would be classified as Type 1 than there are for fainter objects. Recent discussions in the literature suggest that this might be the case. Elitzur et al. (2014) extended the analysis of Elitzur & Ho (2009) and confirmed the viability of a model where AGN broad-line emission follows an evolutionary sequence from Type 1 to 2 as the accretion rate onto the central black hole is decreasing. The authors suggest that the (at least partially) controlling parameter of this spectral evolution and the torus opening angle is $L_{Bol}/M^{2/3}$, that is only a function of L for the $M = \text{const.}$ case.

On the other hand, at fixed Eddington ratio (i.e., along a column in Figure 13), the allowed region decreases from top to bottom, i.e., with increasing mass. The Elitzur et al. (2014) results could be interpreted as implying that under fixed Eddington ratio conditions the torus opening angle (measured from the axis) should increase with decreasing mass. That can be seen by rewriting the Elitzur et al. (2014) parameter in terms of the Eddington ratio as $L_{Bol}/M^{2/3} = (L_{Bol}/M) M^{1/3} \propto (L_{Bol}/L_{Edd}) M^{1/3} = \dot{m} M^{1/3}$. As mentioned, for the fixed Eddington ratio case, the results for our limits are opposite to Elitzur et al. (2014). However, when considering fixed mass, our results match those of Elitzur et al. (2014). An observational direct realization of such a case was discussed by LaMassa et al. (2015) as a plausible explanation for the “changing look” quasar they discovered.

Note here that, in the case of Elitzur et al. (2014) framework, the decrement in observed broad lines originates in a decreasing accretion rate towards the central engine, that in turn decreases the outflow rate and the object’s bolometric luminosity. At sufficiently low accretion rates, the BLR and the obscuring region are quenched, running out of fuel.

We can also analyse how our findings can be explained in the context of a popular parametrization of the BLR size and the vertical size of the torus that is related to its half-opening angle, σ_t . Some determinations of the vertical size of the torus (e.g., Simpson 2005) provide $h_t \propto L^{1/4}$. We can, then, obtain a crude estimate of the BLR opening using (see e.g., Hönig & Beckert 2007) $\sigma_t \sim h_t/R_{BLR} \propto L^{-1/4}$. Therefore, more luminous objects would have smaller torus openings (measured from the disc). This is in agreement both

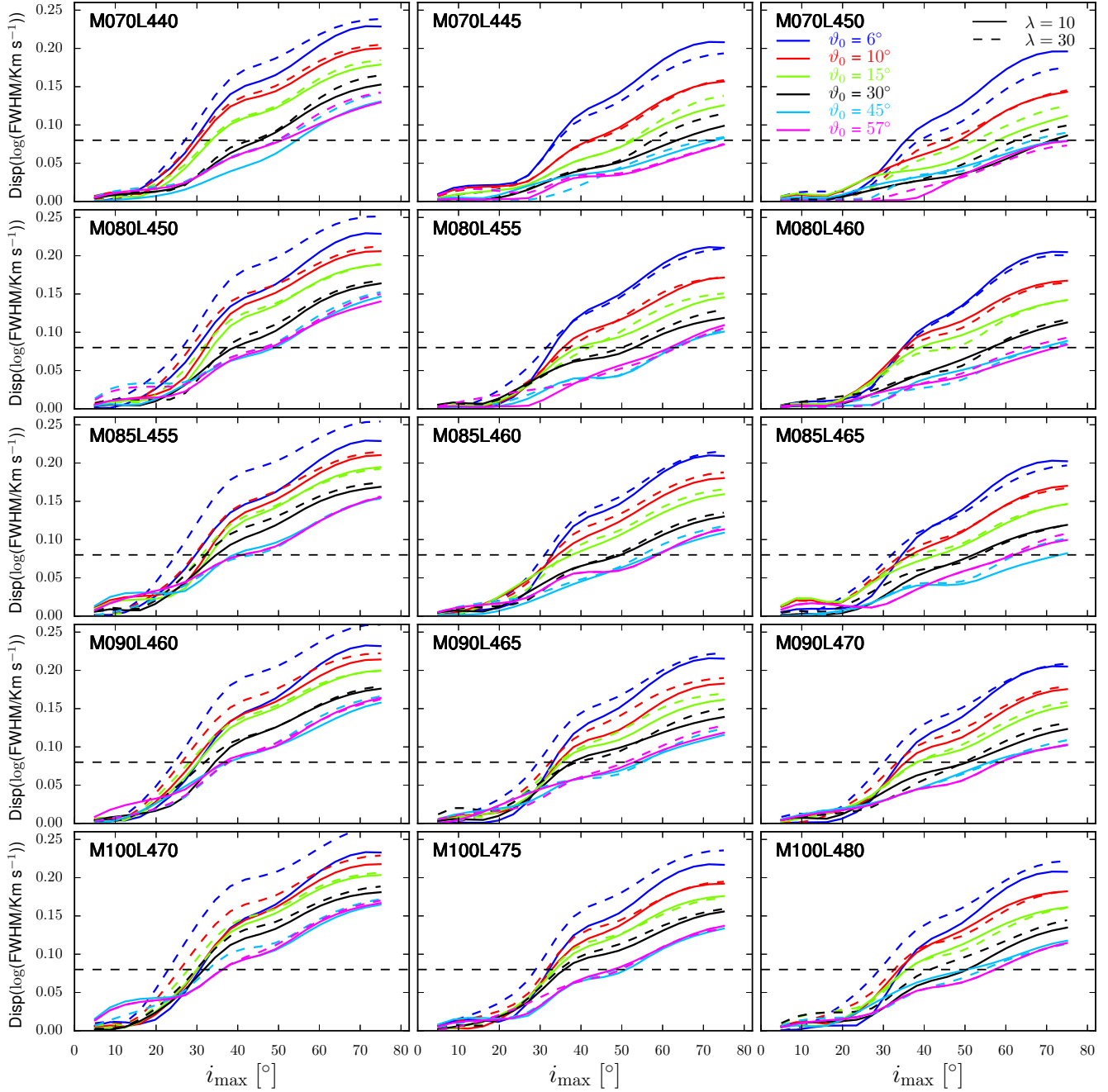


Figure 12. Standard deviation of the profile FWHM vs. inclination angle. Each panel corresponds to a different combination of mass and luminosity and each line represent results for a given launch angle. The black horizontal dashed line corresponds to the [Fine et al. \(2010\)](#) 0.08 dex constraint.

with our results (at $M = \text{const.}$) and those of [Elitzur et al. \(2014\)](#).

The dependence of the torus height on luminosity is a modification suggested by [Simpson \(2005\)](#) to the model known as “receding torus”, proposed by [Lawrence \(1991\)](#), wherein the height of the torus is constant as a function of radius. As discussed in the recent review by [Bianchi et al. \(2012\)](#), this dependence of the obscuring structure covering factor on the luminosity has been supported by many observational results, in different wavelengths. For instance, hard

X-ray studies (e.g., [Ueda et al. 2003](#); [Akylas et al. 2006](#); [Tozzi et al. 2006](#)) and in the optical (e.g., [Arshakian 2005](#); [Simpson 2005](#); [Polletta et al. 2008](#)). [Treister & Urry \(2012\)](#); [Alonso-Herrero et al. \(2011\)](#) and more recently [Oh et al. \(2015\)](#) also show results consistent with the receding torus model. Other authors, on the other hand, do not favour it. [Lawrence & Elvis \(2010\)](#), for instance, have questioned the validity of the above results, arguing that, at least in optical and IR-selected samples, such a luminosity dependence is an

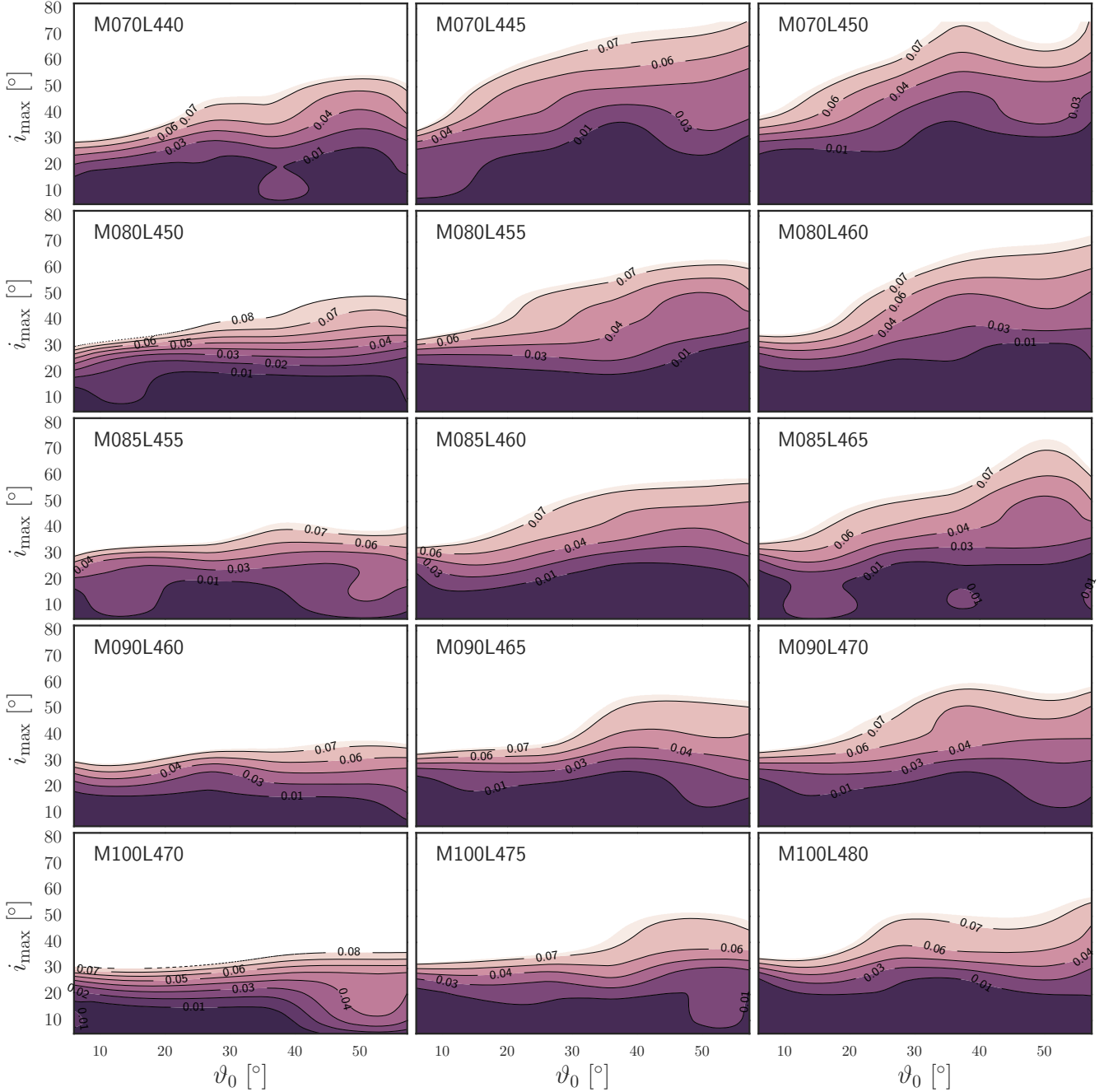


Figure 13. Contour plot of the standard deviation of the profile FWHM vs. launch and maximum inclination angles, for the $\lambda = 10$ case. Only the contours within the region matching the [Fine et al. \(2010\)](#) results are shown. Each panel corresponds to a different combination of mass and luminosity, labelled according to the adopted convention, as described in the caption to [Figure 3](#).

artifact due to the adopted definition of “obscured” and to the inclusion of low excitation AGN.

4.3 Dispersion of log FWHM-Clumpy torus

In clumpy torus models, the obscuring structure is discrete, consisting of optically thick clouds and the quasar is obscured when one such cloud is seen along the LoS. We start by briefly recalling the main characteristics of clumpy tori (e.g., [Nenkova et al. 2008](#); [Mor et al. 2009](#)). In such a model,

the torus is characterised by the inner radius of the cloud distribution (set to the dust sublimation radius, R_d , that depends on the grain properties and mixture) and six other parameters. These are the outer radius, R_o ; the viewing angle i ; the torus width parameter (analogous to its opening angle), σ ; the mean number of clouds along a radial equatorial line, N_0 ; the optical depth per cloud, τ_v (the same for all clouds in the configuration) and the power-law index of radial density profile, q , such that the number of clouds follows $N(r) \propto r^{-q}$. Note that the outer radius is often given

through the alternative parameter $Y = R_o/R_d$. An implicit assumption is that the disc and torus are aligned.

Equation (3) in [Mor et al. \(2009\)](#) provides the escape probability associated with a soft-edge clumpy torus prescription with a Gaussian distribution, that we include below for completeness

$$P_{\text{esc}}(i) = \exp \left[-N_0 \exp \left(-\frac{(90^\circ - i)^2}{\sigma^2} \right) \right]. \quad (17)$$

Authors that support a clumpy rather than a smooth dust distribution torus (e.g., [Hönig & Beckert 2007](#); [Nenkova et al. 2008](#)) argue that the decreasing fraction of Type 2 objects at high luminosities discussed in section 4.2 depends not only on the decreasing torus opening angle, but also on the decreasing N_0 . The torus “covering factor” f_2 is estimated by the fraction of Type 2 sources in the total population (e.g., [Lawrence & Elvis 2010](#)) and is related to the torus half-opening angle according to $f_2 = 1 - \int_0^{\pi/2} P_{\text{esc}}(i) \sin i \, di$. For a smooth torus, this factor is given by $f_2 = \sin \sigma_t$ but it is modified and becomes a function of the number of cloudlets if a clumpy torus is considered.

In Figure 14 we show the standard deviation of the profile FWHM vs. launch angle obtained from our line profiles for the [Nenkova et al. \(2008\)](#) clumpy torus formulation. Note that as we have adopted the soft-edge case of the model, only $i_{\text{max}} = 90^\circ$ is needed. Hence, the plots are curves and not contour levels. Each panel corresponds to a different combination of mass and luminosity and each line represents results for a different value of the torus model parameters σ_t and N_0 adopted from the [Mor et al. \(2009\)](#) sample. The black horizontal dashed line is the [Fine et al. \(2010\)](#) 0.08 dex constraint.

As in Figure 13, the mass is constant along rows and the accretion rate is constant along columns. As in the smooth torus case, we find that the agreement (or lack thereof) with the observational constraint depends on the mass and the accretion rate separately, with better agreement (i.e., reached from a smaller ϑ_0 angle) achieved for the lowest mass and larger Eddington ratio. Indeed, at the lowest \dot{m} , there is no combination of parameters that satisfies the condition imposed. Additionally, the curves corresponding to larger N_0 cross the limiting line at smaller ϑ_0 . That is, our results favour denser structures.

5 COMPARING RESULTS FOR DIFFERENT λ VALUES

In previous sections we have shown that the line profiles, and so their FWHMs and corresponding dispersions, depend only weakly on the dimensionless angular momentum parameter. Here we discuss this result in terms of the velocity and magnetic fields governing the line formation in the framework of our model. Recall that, within the ideal MHD formalism of wind launching sketched in Section 2.1.2, the angular momentum l is constant along a field line (and so is its dimensionless version λ). Moreover, as also discussed in that Section, in the [EBS92](#) model (and, therefore in ours), the adopted free parameters are λ and ϑ_0 , while κ is related to λ by a nonlinear correspondence, shown in Equation (12). If we consider cases of equal masses and luminosities but different λ , and additionally assume same launch angles (i.e.,

same ξ'_0 values) and density structures, we can see that the difference is due only to differences in the magnetic fields. In effect, equal masses imply equal Keplerian velocities, which in turn implies that the differences in the parameter k values can only be due to the magnetic field. Furthermore, equal masses also imply that the radial structure in the two cases are identical, so the difference in λ is only related to the poloidal variable ξ .

Comparing the profiles presented in Figures 3 to 5, it is evident that the differences in shape and line-width between results based on the two different λ values adopted depend on ϑ_0 but very mildly (if at all) on the viewing angle. For $i = \text{const.}$, the difference is maximum for the minimum adopted value of ϑ_0 and becomes negligible as the parameter increases. For $\vartheta_0 = \text{const.}$, the difference between profiles remain fairly constant along the whole range. There are a few departures, generally at the lowest ϑ_0 and for the smallest i , but those do not invalidate the general behaviour.

Similarly, the shapes and FWHMs show maximum differences for $\vartheta_0 = 6^\circ$ and almost negligible for larger ϑ_0 s, as can be seen from Figure 7. The dispersion of linewidths, plotted in Figure 12, show also that the larger differences occur, in general, at smaller ϑ_0 values, with a few cases where noticeable differences are seen at large ϑ_0 angles.

The question is, then, why the results from the two different λ values seem to be more distinguishable for smaller ϑ_0 ? To analyse the issue, we will exploit the independence of the differences between profiles on viewing angle mentioned above. Note that, for given M and L , these differences are also independent of ν . The above features allow us to choose convenient values for both frequency and i that will simplify the analysis. We therefore adopt $\nu = \nu_D$ and $i = 0^\circ$ (although this particular viewing angle was not part of the simulations, the independence referred to allows this choice). Adopting $\nu = \nu_D$ gives, replacing in Equations (3) and (4), $e_\nu = e_{\nu_D} = 1$ and $x_\nu = x_{\nu_D} = 0$, respectively. Therefore, the optical depth, that is constructed using Equations (2) to (4) as $\tau_\nu = \tau e_\nu e^{-x_\nu^2}$, is simplified to $\tau_\nu = \tau_{\nu_D} = \tau$. We also have $\nu_D(i = 0^\circ) = v_p \sin \vartheta$.

To evaluate τ_{ν_D} we need to determine Q and q_{tt} appropriate for the chosen frequency and viewing angle values. The expression of Q is given in [Paper I](#). For $i = 0^\circ$, it simplifies to $Q = \Lambda_{zz} = \frac{\partial v_z}{\partial z}$. In the framework of the [EBS92](#) solution to the MHD equations, this derivative is given by $\sqrt{\frac{GM}{r_0^3}} \left[\frac{f+4f'(\chi+c_2)}{2(\chi+2c_2)} \right]$. The first factor is independent of λ and ϑ_0 , we can therefore concentrate only on the second factor. Recall that the profiles were obtained through quantities evaluated at $z = z_{\text{em}}$. Therefore, $Q(\chi = \chi_{\text{em}}) \propto \left[\frac{f(\chi_{\text{em}})+4f'(\chi_{\text{em}})(\chi_{\text{em}}+c_2)}{2(\chi_{\text{em}}+2c_2)} \right]$. The leading factor of the dependence of the function $f(\chi)$ and its derivative on λ is f_∞ , introduced in Equation (10). This gives

$$Q \sim \frac{f_\infty}{2(\chi_{\text{em}} + 2c_2)} = \sqrt{\frac{2\lambda - 3}{3}} \frac{1}{2(\chi_{\text{em}} + \tan \vartheta_0)}. \quad (18)$$

Note that q_{tt} is intrinsically independent of λ . Thus, for the dependence on λ , Q is the dominant term and we have, then, that the optical depth $\tau \sim Q^{-1}$ decreases when λ increases. As $L_\nu \propto 1 - e^{-\tau}$, we have then shown that the luminosity would be larger for smaller λ . In addition, due to the term containing $\tan \vartheta_0$ in the numerator of Equation (18), the difference decreases with increasing ϑ_0 .

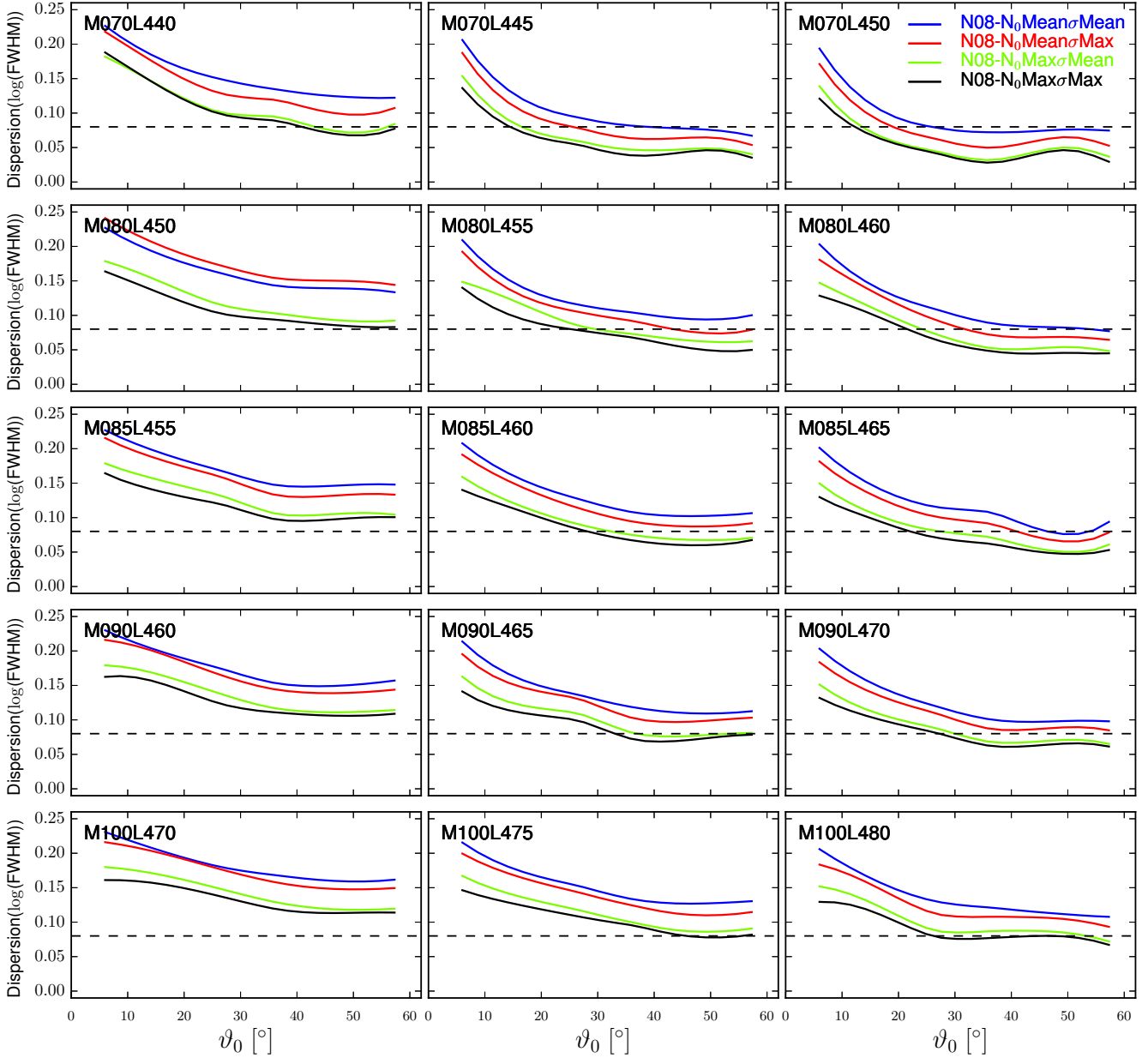


Figure 14. Standard deviation of the profile FWHM vs. launch angle, using the [Nenkova et al. \(2008\)](#) clumpy torus prescription. The black horizontal dashed line corresponds to the [Fine et al. \(2010\)](#) 0.08 dex constraint. Each panel corresponds to a different combination of mass and luminosity and each line represent results for a given launch angle.

6 DISCUSSION

Considering the $\log L$ - \log FWHM plane in Figure 8 and the contour plots of $\text{Disp}(\log \text{FWHM})$ in Figure 13 we would like to assess which parameter(s), and in which direction(s), should be changed in future simulations to achieve better agreement with the observational results.

Note first that the angle i_{\max} used throughout this work is measured from the polar axis (i.e. it is the complementary to the angle $\sigma_t = \tan^{-1} h_t/r_t$ defined above). The receding torus model posits that the i_{\max} parameter of more luminous objects is larger. Indeed, for constant mass our results permit that trend, although they hint that the torus opening angle of more luminous objects is smaller than that of fainter

counterparts. But, as mentioned in Section 4.2, at fixed mass the trend is that reported by [Elitzur et al. \(2014\)](#), i.e., that the torus opening angle decreases with luminosity. These points suggest that our model is, in its general conception, adequate although some of the parameter choices have to be reviewed for it to better represent real cases.

For example, the tilt of the emitting region with respect to the equatorial plane was chosen to match that of [MC97](#), which was in turn chosen based on a BAL quasar fraction of ~ 0.1 , a value that has been updated ([Allen et al. 2011](#)). More recent values put the BAL fraction as large as ~ 0.25 of the quasar population, implying an emission region with a steeper slope. In such a case, the effective length over which

the emission is obtained would increase and be at higher distances above the disc. This would affect both the velocities and their derivatives, thus affecting Q and the optical depth, ultimately modifying the FWHM of the line profiles, but perhaps not as much their shapes. Here we recall that this slope can be a function of the radius, as opposed to the fixed value adopted in this work. Adopting a function that smoothly increases with radius (similar to the bowl-shaped BLR geometry in the model proposed by Goad et al. (2012)) instead of a constant slope, would make the streamlines intercept the emission region at higher heights from the disc plane, which would produce broader profiles, and probably with more dispersion. A related description of the BLR structure, described as “nested rings” geometry, was proposed by Mannucci et al. (1992) and later reintroduced by Gaskell and collaborators (e.g., Gaskell et al. 2008; Gaskell 2009). Either of these geometries could provide a constraint to the families of possible curves to adopt as the base of the emission region.

The spatial profile of the density could be reviewed or adjusted, too. Here we have to consider both the radial and the vertical structures, that are decoupled in the adopted model. As discussed in Section 2, the density structure in the radial direction is such that $n(r) \propto r^{-2}$, but a closer value to the corresponding Shakura & Sunyaev (1973) relevant accretion disc region would be a power-law exponent $-3/2$. Other possibilities involve changing the underlying disc model, adopting, e.g., a slim disc instead of the geometrically thin and optically thick disc of Shakura & Sunyaev (1973). Slim discs were developed in the pseudo-Newtonian limit by Abramowicz et al. (1988) and are more suitable for larger accretion rates ($\dot{m} \gtrsim 0.3$, e.g., Abramowicz & Fragile (2013)).

In the z direction, the density drops off away from the base of the emission according to a half-Gaussian dependence, regulated by both the height and the thickness of the emission region. The former depends on the geometry of the region, discussed in the previous paragraph. Any modification to the latter should still ensure that it satisfies $l_{\text{em}} \ll z_{\text{em}}$. The radial size of the line-emitting region, given by the ratio $r_{\text{max}}/r_{\text{min}}$, was fixed throughout the present work. However, the amount of line shift and the degree of asymmetry of the line profiles are functions of it (e.g., Flohic et al. 2012). Therefore, it would be important to effectively study how this parameter affects the results.

The turbulent velocity has been chosen to be constant, but it also can depend on the radial coordinate. For instance, it has been shown that magnetorotational instability (MRI, Balbus & Hawley 1991) provides a plausible mechanism to develop turbulence and transport angular momentum in discs, due to their differential Keplerian rotation.

Another point to consider is that we did not explore changes in the photoionization calculations. The CLOUDY runs yielding the source function results used in this work were obtained adopting specific prescriptions for the various parameters in the code that define the photoionization state of the gas. The ionization and excitation structure of the gas depend on the spectral energy distribution (SED), the number density n_γ of ionizing photons irradiating the gas, the metallicity and number density n of the gas (e.g., MC98). The ionization parameter, defined as $U = n_\gamma/n$ encapsulates several of these quantities and is a convenient way to

describe the ionization state of the medium. Thus,

$$U = \frac{1}{4\pi r^2 c n_{\text{H}}} \int_{\nu_0}^{\infty} \frac{L_\nu}{h\nu} d\nu = \frac{Q_{\text{H}}}{4\pi r^2 n c}, \quad (19)$$

where ν_0 is the threshold ionization frequency, h is Planck’s constant, n is the hydrogen number density and $Q_{\text{H}} = \int_{\nu_0}^{\infty} \frac{L_\nu}{h\nu}$ is the rate of ionizing photons emitted by the source. Values $U > 1$ indicate a highly ionized gas, while the gas is in low-ionization state for $U < 1$.

Changes in the adopted prescription of any (or all) of these parameters will lead to a different structure of the gas and its ionization and excitation states, in the disc and wind. For example, for most of their model cases Murray & Chiang (1997, 1998) employed a (modified in the X-ray region) Mathews & Ferland (1987) SED, that is still very popular in the literature. Adopting a different SED would affect the ionization structure in the wind, but in a wind scenario there is not total freedom in choosing an alternative. A distribution too strong in X-rays compared with the UV portion may preclude the formation of a wind, because the gas is overionized before it can be accelerated. In such a case, the higher ionization lines, such as CIV, would instead be produced in the low-velocity gas, that is illuminated by a continuum that is now strong in the extreme UV and in the X-rays (Leighly 2004).

In section 2.1.2 we mentioned that our work does not account for scattering effects. However, the importance of this process has been recently highlighted by Higginbottom et al. (2014) who, using Monte-Carlo radiative transfer simulations, showed that including scattering of ionizing photons leads to a very high ionization parameter and modifies the outflow emission properties.

7 SUMMARY AND CONCLUSIONS

In this work we have studied AGN broad emission line profiles with a model that combines an improved version of the accretion disc wind model of Murray & Chiang (1997) with the hydromagnetic driving of Emmering et al. (1992). The dynamics of these self-similar MHD outflows is characterised by two parameters, e.g., the dimensionless angular momentum λ , and the wind-launch angle with respect to the disc plane ϑ_0 .

We have compared the dispersions in our model CIV linewidth distributions to observational upper limits on that dispersion. Those limits translate to an upper limit to the half-opening angle of the putative torus feature that is part of the standard model describing the AGN phenomenon. To achieve this, we constructed contour plots of the dispersion of $\log(\text{FWHM})$ in the $\vartheta_0 - i_{\text{max}}$ plane, capped with the Fine et al. (2010) observed upper limit dispersion, defining in this way a boundary line i_{max} vs ϑ_0 , below which an object can be seen as Type 1.

The maximum torus half-opening angle of about 47° reported in Paper I has been corrected. That value was obtained based on an erroneous interpolation routine of the CLOUDY-generated source function points. The revised maximum torus half-opening angle is larger, about 75° . In fact, the maximum torus half-opening angle is an increasing function of the wind launch angle ϑ_0 .

We extended the analysis presented in Paper I to consider a range of black hole masses and luminosities. In a similar manner to the approach adopted in the fiducial case, we computed, for different combinations of mass and luminosity of the central object within that range, line profiles corresponding to the same combinations of wind-launch and viewing angles used before. Additional series of model runs with different values of λ suggest that the profile linewidths and corresponding dispersions depend only mildly on this parameter.

We also found that many of the profile line characteristics, such as the FWHM, the (blue- or red-) shift with respect to the systemic velocity, and the degree of asymmetry, depend not only on the viewing angle (a parameter external to the object, depending on the orientation of the observer relative to the source), but also on the launch angle ϑ_0 , a parameter that is intrinsic to the object. Additionally, our results suggest that large values of ϑ_0 are preferred.

The analysis of the luminosity-linewidth relation showed that the black hole masses could not be recovered if the relation proposed by VP06 (reproduced in Equation (14)) is applied. While this discrepancy could be due to the FWHM of our line profiles, it would be worth evaluating if the inclusion of new empirical data from the literature supports the view that the expression needs to be reconsidered.

We then studied, for each case, the dispersion of $\log(\text{FWHM})$ and imposed the observational results of Fine et al. (2010). Again, contour plots of the dispersion of $\log(\text{FWHM})$ in the $\vartheta_0 - i_{\max}$ plane, constrained with the Fine et al. (2010) results, were used to determine the torus half-opening angle appropriate for each case. The picture that emerged is that the dispersion of the linewidth depends on both the mass of the central object and the Eddington ratio at which it is fed. At fixed mass, the maximum allowed torus half-opening angle (measured from the axis) increases with increasing Eddington ratio (equivalent, under the fixed mass condition, to increasing luminosity). That can be interpreted as objects with larger accretion rates having a higher probability of being observed as Type 1 AGN than those fed at a lower rate. At fixed Eddington ratio, the probability that an object will be seen as Type 1 decreases with increasing mass. But the timescales for mass changes due to accretion are larger enough for any particular system to be considered of constant mass, and, as mention above, in that scenario our results are in agreement with the observational report of Elitzur et al. (2014).

A clumpy torus was also analysed. The limiting viewing angle to integrate over this was always 90° , as opposed to the differential i_{\max} that was used in the putative smooth torus case. Except for this difference, this alternative obscuring structure yielded similar constraints to those obtained with the traditional torus. Moreover, the results favour denser structures.

Ultimately, this work links theory with observational results, by imposing an observational constraint to the distribution of a property of the emission lines emerging from the BLR. The BLR is modelled through a physically well motivated wind description and the observational constraint on the dispersion of the line-width distribution allows it to be translated into a constraint on the geometry of the obscuring structure that is invoked to explain the Type 1/Type 2 dichotomy among AGNs.

ACKNOWLEDGMENTS

LSC and PBH acknowledge support from NSERC. The authors would like to thank the anonymous referee for very helpful comments and suggestions.

REFERENCES

- Abramowicz M. A., Fragile P. C., 2013, *Living Reviews in Relativity*, **16**
- Abramowicz M. A., Czerny B., Lasota J. P., Szuszkiewicz E., 1988, *ApJ*, **332**, 646
- Akylas A., Georgantopoulos I., Georgakakis A., Kitsionas S., Hatziminaoglou E., 2006, *A&A*, **459**, 693
- Allen J. T., Hewett P. C., Maddox N., Richards G. T., Belokurov V., 2011, *MNRAS*, **410**, 860
- Alonso-Herrero A., et al., 2011, *ApJ*, **736**, 82
- Arshakian T. G., 2005, *A&A*, **436**, 817
- Assef R. J., et al., 2011, *ApJ*, **742**, 93
- Balbus S. A., Hawley J. F., 1991, *ApJ*, **376**, 214
- Bianchi S., Maiolino R., Risaliti G., 2012, *Adv. Astron.*, 2012, 782030
- Blandford R. D., Payne D. G., 1982, *MNRAS*, **199**, 883
- Bottorff M., Korista K. T., Shlosman I., Blandford R. D., 1997, *ApJ*, **479**, 200
- Chajet L. S., Hall P. B., 2013, *MNRAS*, **429**, 3214
- Chelouche D., Zucker S., 2013, *ApJ*, **769**, 124
- Collin S., Kawaguchi T., Peterson B. M., Vestergaard M., 2006, *A&A*, **456**, 75
- Contopoulos J., Lovelace R. V. E., 1994, *ApJ*, **429**, 139
- Decarli R., Labita M., Treves A., Falomo R., 2008, *MNRAS*, **387**, 1237
- Decarli R., Falomo R., Treves A., Kotilainen J. K., Labita M., Scarpa R., 2010, *MNRAS*, **402**, 2441
- Denney K. D., 2012, *ApJ*, **759**, 44
- Elitzur M., Ho L. C., 2009, *ApJ*, **701**, L91
- Elitzur M., Ho L. C., Trump J. R., 2014, *MNRAS*, **438**, 3340
- Elvis M., 2000, *ApJ*, **545**, 63
- Emmering R. T., Blandford R. D., Shlosman I., 1992, *ApJ*, **385**, 460
- Eracleous M., 2006, in Gaskell C. M., McHardy I. M., Peterson B. M., Sergeev S. G., eds, *Astronomical Society of the Pacific Conference Series Vol. 360*, Astronomical Society of the Pacific Conference Series. p. 217
- Eracleous M., Halpern J. P., 2003, *ApJ*, **599**, 886
- Everett J. E., 2005, *ApJ*, **631**, 689
- Everett J. E., 2007, *Ap&SS*, **311**, 269
- Fine S., et al., 2008, *MNRAS*, **390**, 1413
- Fine S., Croom S. M., Bland-Hawthorn J., Pimblet K. A., Ross N. P., Schneider D. P., Shanks T., 2010, *MNRAS*, **409**, 591
- Flohic H. M. L. G., Eracleous M., Bogdanović T., 2012, *ApJ*, **753**, 133
- Gaskell C. M., 2009, *New Astron. Rev.*, **53**, 140
- Gaskell C. M., Goosmann R. W., Klimek E. S., 2008, *Mem. Soc. Astron. Italiana*, **79**, 1090
- Goad M. R., Korista K. T., Ruff A. J., 2012, *MNRAS*, **426**, 3086
- Grier C. J., et al., 2013, *ApJ*, **764**, 47
- Gültekin K., et al., 2009, *ApJ*, **698**, 198
- Häring N., Rix H.-W., 2004, *ApJ*, **604**, L89
- Heyvaerts J., 1996, in Chiuderi C., Einaudi G., eds, *Lecture Notes in Physics*, Vol. 468, *Plasma Astrophysics*. Springer Berlin / Heidelberg, pp 31–99, <http://dx.doi.org/10.1007/BFb0102542>
- Higginbottom N., Proga D., Knigge C., Long K. S., Matthews J. H., Sim S. A., 2014, *ApJ*, **789**, 19
- Hönig S. F., Beckert T., 2007, *MNRAS*, **380**, 1172

- Kaspi S., Brandt W. N., Maoz D., Netzer H., Schneider D. P., Shemmer O., 2007, *ApJ*, 659, 997
- Kazanas D., Fukumura K., Behar E., Contopoulos I., Shrader C., 2012, *The Astronomical Review*, 7, 92
- Königl A., Kartje J. F., 1994, *ApJ*, 434, 446
- Kurosawa R., Proga D., 2009, *MNRAS*, 397, 1791
- LaMassa S. M., et al., 2015, *ApJ*, 800, 144
- Lawrence A., 1991, *MNRAS*, 252, 586
- Lawrence A., Elvis M., 2010, *ApJ*, 714, 561
- Leighly K. M., 2004, *ApJ*, 611, 125
- Mannucci F., Salvati M., Stanga R. M., 1992, *ApJ*, 394, 98
- Marconi A., Hunt L. K., 2003, *ApJ*, 589, L21
- Mathews W. G., Ferland G. J., 1987, *ApJ*, 323, 456
- Mestel L., 1968, *MNRAS*, 138, 359
- Mor R., Netzer H., Elitzur M., 2009, *ApJ*, 705, 298
- Murray N., Chiang J., 1997, *ApJ*, 474, 91
- Murray N., Chiang J., 1998, *ApJ*, 494, 125
- Murray N., Chiang J., Grossman S. A., Voit G. M., 1995, *ApJ*, 451, 498
- Nenkova M., Sirocky M. M., Ivezić Ž., Elitzur M., 2008, *ApJ*, 685, 147
- Oh K., Yi S. K., Schawinski K., Koss M., Trakhtenbrot B., Soto K., 2015, *ApJS*, 219, 1
- Peterson B. M., Wandel A., 2000, *ApJ*, 540, L13
- Polletta M., Weedman D., Hönig S., Lonsdale C. J., Smith H. E., Houck J., 2008, *ApJ*, 675, 960
- Richards G. T., 2012, in Chartas G., Hamann F., Leighly K. M., eds, *Astronomical Society of the Pacific Conference Series Vol. 460, AGN Winds in Charleston*. p. 67 ([arXiv:1201.2595](https://arxiv.org/abs/1201.2595))
- Rybicki G. B., Hummer D. G., 1978, *ApJ*, 219, 654
- Rybicki G. B., Hummer D. G., 1983, *ApJ*, 274, 380
- Shakura N. I., Sunyaev R. A., 1973, *A&A*, 24, 337
- Simpson C., 2005, *MNRAS*, 360, 565
- Sluse D., et al., 2011, *A&A*, 528, A100
- Sulentic J. W., Marziani P., Dultzin-Hacyan D., Calvani M., Moles M., 1995, *ApJ*, 445, L85
- Sulentic J. W., Marziani P., Dultzin-Hacyan D., 2000, *ARA&A*, 38, 521
- Tozzi P., et al., 2006, *A&A*, 451, 457
- Treister E., Urry C. M., 2012, *Advances in Astronomy*, 2012, 516193
- Ueda Y., Akiyama M., Ohta K., Miyaji T., 2003, *ApJ*, 598, 886
- Vanden Berk D. E., et al., 2001, *AJ*, 122, 549
- Vestergaard M., Peterson B. M., 2006, *ApJ*, 641, 689

This paper has been typeset from a $\text{\TeX}/\text{\LaTeX}$ file prepared by the author.